IEEE Access
Multidisciplinary | Rapid Review | Open Access Journal

Received November 8, 2021, accepted December 12, 2021, date of publication December 14, 2021,
date of current version December 27, 2021.

Digital Object Identifier 10.1109/ACCESS.2021.3135663

Design and Analysis of In-Band Full-Duplex Private 5G Networks Using FR2 Band

HAIFENG LUO, ABHIJEET BISHNU, (Member, IEEE), AND THARMALINGAM RATNARAJAH, (Senior Member, IEEE)
Institute for Digital Communications, School of Engineering, The University of Edinburgh, Edinburgh EH9 3FG, U.K.

Corresponding author: Haifeng Luo (s1895225@ed.ac.uk)

The work of Haifeng Luo and Abhijeet Bishnu was supported in part by the research grant from Huawei Technologies Canada Company Ltd., and in part by Huawei Technologies (Sweden) AB. The work of Tharmalingam Ratnarajah was supported by the U.K. Engineering and Physical Sciences Research Council (EPSRC) under Grant EP/P009549/1.

ABSTRACT This paper studies a solution for efficient industrial Internet of things (IIoT) communications through an in-band full-duplex (IBFD) enabled private 5G network in frequency range 2 (FR2) band ($\geq$ 24.250 GHz), where ultra-reliable low-latency communications (URLLC) and enhanced mobile broadband (eMBB) devices can be simultaneously served. Large-scale antenna array and RF beamforming are applied, and a self-interference cancellation (SIC) scheme is proposed under such architecture. Particularly, the proposed RF cancellation scheme addressed two key issues of extending current technologies to wideband operations in FR2 band: limited operational bandwidth and the requirement for a large number of cancellers. Then, a frequency domain-based digital canceller is proposed to process with the residual self-interference (RSI) with short processing latency. A game theoretic user allocation algorithm is proposed to minimise co-channel interference (CCI) in a heterogeneous environment. Given a typical IIoT scenario, the performance of such IBFD private 5G network is evaluated in terms of bit error rate (BER) and spectral efficiency (SE) through simulations and analysed based on numerical results and theoretical calculations. It is demonstrated that the latency of uplink eMBB devices can be reduced by 54% through IBFD radios, and the latency of downlink URLLC devices can be reduced to 0.5 ms with the help of flexible numerology, mini-slot, and self-contained sub-frames introduced in 5G NR. IBFD radios can enhance the SE by 92% compared to HD radios with our SIC and user allocation policy. The high SE in conjunction with abundant resources in FR2 band provides multi-Gbps peak data rates, high reliability, and massive connectivity.

INDEX TERMS Co-channel interference, FR2 band, in-band full-duplex, IIoT, private 5G network, self-interference cancellation.

I. INTRODUCTION

5G and beyond is particularly attractive for industrial communications due to its unified wireless interface, guaranteed quality of service, mobility, security, and positioning [1]. Different from traditional human-centric communication networks, industrial Internet of things (IIoT) need to serve multi-type devices for diverse applications, e.g., ultra-reliable low-latency communications (URLLC) devices for control applications, enhanced mobile broadband (eMBB) devices for bandwidth-hungry applications, and massive machine-type communications (mMTC) devices for monitoring applications [2], [3]. In order to cope up with such a heterogeneous environment, various requirements are introduced in 5G new radio (NR) such as ultra-high reliability, low latency, high connection density, high energy and spectral efficiency, and high flexibility [3]. In particular, the URLLC service is the most challenging due to simultaneous requirements on ultra-high reliability and low latency with limited resources.

To meet the stringent demand of huge capacities and low latency in 5G and beyond IIoT networks, the in-band full-duplex (IBFD) radios and frequency range 2 (FR2) spectrum ($\geq$ 24.250 GHz), i.e., millimeter wave (mmWave), are investigated as promising techniques [4]–[7]. IBFD is a novel paradigm that allows simultaneous transmission and reception in the same frequency band, so it has the potential

The associate editor coordinating the review of this manuscript and approving it for publication was Usama Mir.

to enhance the spectrum efficiency and reduce the latency of current time division duplex (TDD) or frequency division duplex (FDD) systems [8]. FR2 provides much more unused spectrum resources than FR1 band ($<$ 7.25 GHz) for high throughput [9], and is considered as a promising technology for eMBB service [3]. For a specific industrial application, the 5G network can be customised and referred to as a local and private 5G network, which enables industrial players to run their own local networks with dedicated equipment [1]. Besides, 5G NR introduces flexible numerology, mini-slot, and self-contained sub-frames concepts to further reduce the latency. The powerful capabilities of 5G NR techniques with the dedicated nature of the local and private 5G network are expected to deliver reliable communications for IIoT, which cannot be achieved by 4G long term evolution (LTE) radios.

Although IBFD and FR2 spectrum provide abundant benefits, there are still problems to be solved in order to realise these technologies in practice. Communications in FR2 band suffers from the weak diffraction ability and susceptibility to blockages due to the short carrier wavelength, resulting in high path loss of communication links [6]. The simultaneous transmission and reception enabled by the IBFD introduce additional interference, i.e., co-channel interference (CCI) from uplink (UL) users to downlink (DL) users and self-interference (SI), which severely degrade the system capacity. These issues have to be appropriately addressed to deliver reliable and efficient IBFD communications in FR2 band. Recent studies have successfully demonstrated optical self-interference cancellation (see [10], [11] and references therein) for efficient active analog SIC, where optical components are explored to construct RF cancellers for more accurate delays and frequency operations. In [12] and [13], conventional polynomial cancellers and novel neural networks-based cancellers are utilised to efficiently bring the residual self-interference close to the receiver noise floor. The processing latency for SIC, which is a significant part of the end-to-end latency, is minimised with considerable reliability in [14] for URLLC. As for the CCI, it is not as significant as the SI due to nature propagation attenuation and can be mitigated simply through interference alignment [15], resource allocation [16] or beamforming [11], [17].

However, these implementations mainly focus on FR1 band within operational bandwidth below 100 MHz, while lacking analysis of extending to FR2 band with a wider bandwidth. Besides, since the private 5G network for IIoT works in a heterogeneous environment, the solutions must be flexible to support a mixture of multi-type devices. In this paper, we propose solutions to solve these challenges under IIoT scenarios. Particularly, a self-interference cancellation (SIC) scheme is proposed to efficiently suppress the significant SI in the analog and digital domain, and a user allocation algorithm is proposed to minimise the CCI. Our solutions are given based on the system model in FR2 band, where large-scale antenna arrays with RF beamforming are utilised to compensate for the high path loss while saving the financial cost and energy consumption. Our contributions are summarised as

- We evaluate the performance of a private 5G NR network equipped with IBFD base stations that provides simultaneous URLLC and eMBB services based on FR2 channel models. We utilise 5G NR 4$\times$ scaled numerology (60 kHz of subcarrier spacing), self-contained sub-frames, and mini-slot for URLLC devices, which could reduce the latency by half while remaining high throughput with the help of abundant resources provided by FR2 band, large-scale antenna array, and IBFD radios. Based on the numerical results of bit-error-rate (BER) and spectral efficiency (SE) and theoretical analysis, the performance of this private 5G network is evaluated in terms of throughput, latency, reliability, and device density.
- We adopt large-scale antenna arrays to compensate for the high path loss in FR2 band and RF beamforming to save the cost and energy through significantly reducing the number of RF chains. Taking advantage of such architecture, we propose to tap the reference signals for RF cancellation from RF chains instead of antennas to reduce the number of RF cancellers, making it practically feasible with large-scale antenna arrays. The effect of the RF beamforming on the SIC with such architecture is firstly analysed in this paper in terms of delay spread.
- We explore optical components to construct a multi-tap RF canceller for a sufficient number of taps and wideband RF signal processing properties at 28 GHz. Compared with existing designs (see [10] and references therein), we considered the processing properties of components for FR2 band and investigated a method to provide sufficient delay lines using normal components instead of elaborate components (e.g., fiber Bragg gratings) to save the cost, which gives a cost-friendly efficient RF cancellation scheme for FR2 band scenarios.
- We investigate a digital canceller that operates in the frequency domain. It captures the effective channel effects by a single coefficient on each subcarrier. Compared with conventional polynomial cancellers as in [14], such canceller has ultra-low processing latency with the help of self-contained sub-frames but lack the ability to deal with nonlinear distortions. The effects of these transceiver and canceller nonlinear distortions on the digital cancellation are analysed.
- The performance of the SIC scheme is analysed and evaluated in terms of cancellation depth, channel estimation accuracy, and overall noise and distortion floor after SIC. This theoretical analysis gives further insights into the SIC under such structure (i.e., large antenna array with RF beamforming).
- We propose a user allocation algorithm to minimise the CCI and maximise the IBFD gain for higher spectral efficiency. Compared with existing methods [16],

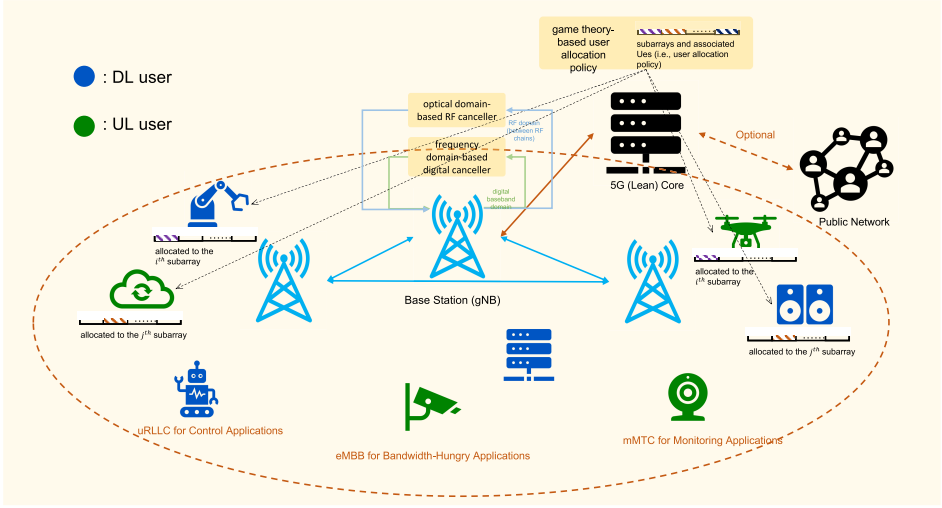

FIGURE 1. A private 5G network for industrial Internet of things applied our solutions.

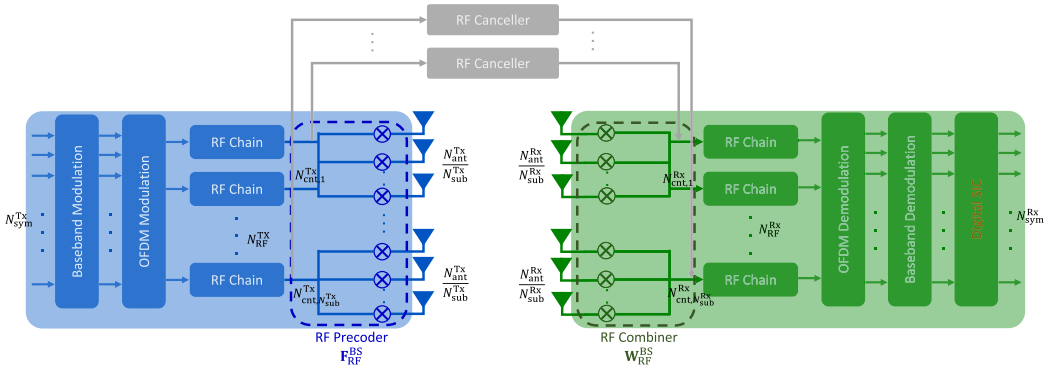

FIGURE 2. A block diagram of the IBFD transceiver applying the SIC and RF beamforming.

we consider the gains of antenna arrays and support for the heterogeneous environment (i.e., multi-type devices with different antenna array sizes and bandwidths), which is more flexible than the existing one and supports antenna arrays. It is analysed that this algorithm can always achieve the optimal allocation policy to minimise the CCI from the perspective of user allocation.

The rest of this paper is organised as follows: Section II gives models of a general FR2 full-duplex private 5G network and a transceiver architecture with RF beamforming, followed by FR2 channel models and end-to-end latency analysis. In Section III, the signal processing for self-interference cancellation in the analog and digital domain is proposed. Then, a user allocation algorithm is proposed to minimise the CCI in Section IV. Section V demonstrates and analyses numerical results of our simulations under a typical IIoT scenario. Finally, conclusions are drawn in Section VI.

II. SYSTEM MODEL

Consider a private 5G network for IIoT as Fig. 1, where K_{BS} IBFD enabled 5G NR base stations (gNB) service K_{DL} DL user equipments (UEs) and K_{UL} UL UEs in FR2 band. To compensate for the high path loss in FR2 band, which is always an obstacle to provide reliable communications [4], [9], large-scale antenna array is leveraged to provide effective links by exploiting the beamforming gain to form highly directional narrow beams. In order to make large-scale antenna array practically feasible, a novel transceiver architecture is utilised as Fig. 2 shows, where RF beamforming is introduced to connect a small amount of RF chains to the large-scale antenna array [5]. Assume each IBFD base station (BS) is equipped with $N_{\mathrm{ant}}^{\mathrm{Tx}}$ and $N_{\mathrm{ant}}^{\mathrm{Rx}}$ transmit and receive antennas connected to $N_{\mathrm{RF}}^{\mathrm{Tx}}$ and $N_{\mathrm{RF}}^{\mathrm{Rx}}$ RF chains respectively, the RF precoder at each BS is a diagonal matrix such as $F_{\mathrm{RF}}^{\mathrm{BS}} = \mathcal{D}\left(f_{\mathrm{RF},1}^{\mathrm{BS}}, \ldots, f_{\mathrm{RF},N_{\mathrm{sub}}^{\mathrm{Tx}}}^{\mathrm{BS}}\right)$ with dimension of $N_{\mathrm{ant}}^{\mathrm{Tx}} \times N_{\mathrm{RF}}^{\mathrm{Tx}}$, where $f_{\mathrm{RF},l}^{\mathrm{BS}}$ has dimension of $\frac{N_{\mathrm{ant}}^{\mathrm{Tx}}}{N_{\mathrm{sub}}^{\mathrm{Tx}}} \times N_{\mathrm{cnt},l}^{\mathrm{Tx}}$, $N_{\mathrm{sub}}^{\mathrm{Tx}}$ is the fixed number of subarrays of the transmit antenna array and $N_{\mathrm{cnt},l}^{\mathrm{Tx}}$ is the variable number of RF chains connected to the l^{th} subarray. It should be noted that the RF precoding is achieved via phase shifters in practice, so that we have $\left|[f_{\mathrm{RF}}^{\mathrm{BS}}]_{m,n}\right|^2 = 1$. Similarly, the RF combiner matrix is given

as $W_{\mathrm{RF}}^{\mathrm{BS}} = \mathcal{D}\left(w_{\mathrm{RF},1}^{\mathrm{BS}}, \ldots, w_{\mathrm{RF},N_{\mathrm{sub}}^{\mathrm{Rx}}}^{\mathrm{BS}}\right) \in \mathbb{C}^{N_{\mathrm{ant}}^{\mathrm{Rx}} \times N_{\mathrm{RF}}^{\mathrm{Rx}}}$ and $w_{\mathrm{RF},l}^{\mathrm{BS}}$ has dimension of $\frac{N_{\mathrm{ant}}^{\mathrm{Rx}}}{N_{\mathrm{sub}}^{\mathrm{Rx}}} \times N_{\mathrm{cnt},l}^{\mathrm{Rx}}$, and $\left|[w_{\mathrm{RF}}^{\mathrm{BS}}]_{m,n}\right|^2 = 1$. More details about the RF beamformer are given in Appendix B. The directions of beams are determined by RF precoders and combiners, whose weights can be calculated through fixed positions of UEs or beam management, which consists of beam sweeping, beam measurement, beam determination, and beam reporting (please see our previous work in [4] for more details). Transceivers at UEs have similar architecture and the number of antennas and subarrays are denoted by M for UEs with specific user indicator, e.g., UL user j has $M_{\mathrm{ant},j}^{\mathrm{Tx}}$ transmit antennas. Due to the different requirements of diverse industrial applications, UEs may equip with a different number of antennas and RF chains. A tabular form for the notation used in this paper is given in Appendix A for readers to follow this paper easily.

A. TRANSMITTED SIGNALS

The IBFD base station transmits $N_{\mathrm{sym}}^{\mathrm{Tx}}$ independent data symbols to DL users and receives $N_{\mathrm{sym}}^{\mathrm{Rx}}$ independent data symbols from UL users, respectively. We have $N_{\mathrm{sym}}^{\mathrm{Tx}} = N_{\mathrm{RF}}^{\mathrm{Tx}} \ll N_{\mathrm{ant}}^{\mathrm{Tx}}$ and $N_{\mathrm{sym}}^{\mathrm{Rx}} = N_{\mathrm{RF}}^{\mathrm{Rx}} \ll N_{\mathrm{ant}}^{\mathrm{Rx}}$ to allow the fully-digital beamforming being decomposed into the digital beamforming followed by RF beamforming without penalty [18]. At the BS, the $N_{\mathrm{sym}}^{\mathrm{Tx}}$ modulated data symbols (either by PSK or QAM) at k^{th} subcarrier $s^{\mathrm{BS}}[k]$ are first converted into the time domain by leveraging N_{FFT}-point IFFT followed by addition cyclic prefix. It is then converted into the RF domain by the $N_{\mathrm{RF}}^{\mathrm{Tx}}$ independent RF chains followed by the RF precoder $F_{\mathrm{RF}}^{\mathrm{BS}}$. The transmitted complex symbol from the BS at the k^{th} subcarrier in the discrete frequency-domain is denoted as

$$x^{\mathrm{BS}}[k] = \omega_{\mathrm{BS}}\left(F_{\mathrm{RF}}^{\mathrm{BS}} s^{\mathrm{BS}}[k] + \mathbf{t}^{\mathrm{BS}}[k]\right) \tag{1}$$

where $\mathbb{E}\left\{s^{\mathrm{BS}}[k]\left(s^{\mathrm{BS}}[k]\right)^H\right\} = \frac{P_{BS}}{N_{\mathrm{RF}}^{\mathrm{Tx}}}\mathbf{I}_{N_{\mathrm{RF}}^{\mathrm{Tx}}}$. The vector $\mathbf{t}^{\mathrm{BS}}[k] \in \mathbb{C}^{N_{\mathrm{ant}}^{\mathrm{Tx}} \times 1}$ represents the transmitter distortion caused by RF chains, which can be modelled by a zero mean complex Gaussian distribution as [7]

$$\mathbf{t}[k] \sim \mathcal{CN}\left(0, \sigma_t^2 \mathcal{D}\left(\mathbf{F}_{\mathrm{RF}}[k]\mathbf{s}[k]\mathbf{s}^H[k]\mathbf{F}_{\mathrm{RF}}^H[k]\right)\right) \tag{2}$$

Lastly, ω_{BS} is the scaling factor used to meet the power constraints such that $tr\left(\mathbb{E}\left\{x^{\mathrm{BS}}[k]\left(x^{\mathrm{BS}}[k]\right)^H\right\}\right) = \omega_{\mathrm{BS}}^2\left(1+\sigma_t^2\right)P_{\mathrm{BS}}\frac{N_{\mathrm{ant}}^{\mathrm{Tx}}}{N_{\mathrm{sub}}^{\mathrm{Tx}}} = P_{\mathrm{BS}}$, yielding $\omega_{\mathrm{BS}}^2 = \frac{N_{\mathrm{sub}}^{\mathrm{Tx}}}{(1+\sigma_t^2)N_{\mathrm{ant}}^{\mathrm{Tx}}}$. Similarly, the transmitted complex symbol from the j^{th} UL users at the k^{th} subcarrier in the discrete frequency-domain can be denoted as

$$x_j^{\mathrm{UL}}[k] = \omega_{\mathrm{UL},j}\left(F_{\mathrm{RF}}^{\mathrm{UL},j} s_j^{\mathrm{UL}}[k] + \mathbf{t}_j^{\mathrm{UL}}[k]\right) \tag{3}$$

where $\mathbb{E}\left\{s_j^{\mathrm{UL}}[k]\left(s_j^{\mathrm{UL}}[k]\right)^H\right\} = \frac{P_{\mathrm{UE},j}}{M_{\mathrm{RF},j}^{\mathrm{TX}}}\mathbf{I}_{M_{\mathrm{RF},j}^{\mathrm{TX}}}$, $\omega_{\mathrm{UL},j}^2 = \frac{1}{(1+\sigma_t^2)M_{\mathrm{ant},j}^{\mathrm{Tx}}}$, and the transmitter distortion $\mathbf{t}_j^{\mathrm{UL}}[k]$ is also described by the Gaussian model as Equation (2) (we assume identical transmitter distortion factor σ_t^2 at the BS and UEs for simplicity).

B. RECEIVED SIGNALS

The received signal by BS g at the k^{th} subcarrier can be described as

$$\begin{aligned}
&y_g^{\mathrm{BS}}[k] \\
&= (W_{\mathrm{RF}}^{\mathrm{BS},g})^H H_{g,j_k}^{\mathrm{UL}}[k]\omega_{\mathrm{UL},j_k}\left(F_{\mathrm{RF}}^{\mathrm{UL},j_k} s_{j_k}^{\mathrm{UL}}[k] + \mathbf{t}_{j_k}^{\mathrm{UL}}[k]\right) \\
&\quad + \sum_{b\neq g}^{K_{\mathrm{BS}}} (W_{\mathrm{RF}}^{\mathrm{BS},g})^H H_{g,b}^{\mathrm{BS}}[k]\omega_{\mathrm{BS}}\left(F_{\mathrm{RF}}^{\mathrm{BS},b} s_b^{\mathrm{BS}}[k] + \mathbf{t}_b^{\mathrm{BS}}[k]\right) \\
&\quad + (W_{\mathrm{RF}}^{\mathrm{BS},g})^H H_{\mathrm{SI},g}[k]\omega_{\mathrm{BS}}\left(F_{\mathrm{RF}}^{\mathrm{BS},g} s_g^{\mathrm{BS}}[k] + \mathbf{t}_g^{\mathrm{BS}}[k]\right) \\
&\quad + n_g^{\mathrm{BS}}[k] + n_g^{\mathrm{qtz}}[k] + r_g^{\mathrm{BS}}[k] \\
&= \omega_{\mathrm{UL},j_k}(W_{\mathrm{RF}}^{\mathrm{BS},g})^H H_{g,j_k}^{\mathrm{UL}}[k] F_{\mathrm{RF}}^{\mathrm{UL},j_k} s_{j_k}^{\mathrm{UL}}[k] + \tilde{n}_g^{\mathrm{BS}}[k]
\end{aligned} \tag{4}$$

where $H_{g,b}^{\mathrm{BS}}[k]$, $H_{\mathrm{SI},g}[k]$, and $H_{g,j_k}^{\mathrm{UL}}[k]$ denote the channel coefficients matrix at the k^{th} subcarrier between BSs g and b, the SI channel matrix at BS g, and the UL channel matrix from UL user j_k to BS g, respectively. UL user j_k is the user that occupies the k^{th} subcarrier and transmits the signal of interest, and $\tilde{n}_g^{\mathrm{BS}}[k]$ represents all interference and noise terms except the desired signal. The indexes of RF precoder and combiner are omitted here since it is frequency-flat. There is no intra-user interference since we consider all UEs are orthogonal to each other through appropriate modulations (either by baseband modulation or OFDM). $n_g^{\mathrm{BS}}[k]$ is the additive white Gaussian noise (AWGN) at BS g that $n_g^{\mathrm{BS}}[k] \sim \mathcal{CN}\left(\mathbf{0}, \sigma_{\mathrm{BS}}^2\mathbf{I}_{N_{\mathrm{RF}}^{\mathrm{Rx}}}\right)$, and $n_g^{\mathrm{qtz}}[k]$ denotes the quantisation noise due to limited ADC dynamic range, which will be detailed later. $r_g^{\mathrm{BS}}[k]$ represents the receiver distortions induced by receiver RF chains except the quantisation noise, which can be described by the complex Gaussian model as [7]

$$\mathbf{r}[k] \sim \mathcal{CN}\left(0, \sigma_r^2\mathcal{D}\left(\tilde{\mathbf{y}}[k]\tilde{\mathbf{y}}^H[k]\right)\right) \tag{5}$$

where $\tilde{\mathbf{y}}[k] = \mathbf{y}[k] - \mathbf{r}[k]$ denotes the received signal without receiver distortion. The received signal by DL user i_k at the k^{th} subcarrier is given as

$$\begin{aligned}
&y_{i_k}^{\mathrm{DL}}[k] \\
&= (W_{\mathrm{RF}}^{\mathrm{DL},i_k})^H H_{i_k,b_i}^{\mathrm{DL}}[k]\omega_{\mathrm{BS}}\left(F_{\mathrm{RF}}^{\mathrm{BS},b} s_{b_i}^{\mathrm{BS}}[k] + \mathbf{t}_{b_i}^{\mathrm{BS}}[k]\right) \\
&\quad + \sum_{b\neq b_i}^{K_{\mathrm{BS}}} (W_{\mathrm{RF}}^{\mathrm{DL},i_k})^H H_{i_k,b}^{\mathrm{DL}}[k]\omega_{\mathrm{BS}}\left(F_{\mathrm{RF}}^{\mathrm{BS},b} s_b^{\mathrm{BS}}[k] + \mathbf{t}_b^{\mathrm{BS}}[k]\right) \\
&\quad + (W_{\mathrm{RF}}^{\mathrm{DL},i_k})^H H_{i_k,j_k}^{\mathrm{DU}}[k]\omega_{\mathrm{UL},j_k}\left(F_{\mathrm{RF}}^{\mathrm{UL},j_k} s_{j_k}^{\mathrm{UL}}[k] + \mathbf{t}_{j_k}^{\mathrm{UL}}[k]\right) \\
&\quad + n_{i_k}^{\mathrm{DL}}[k] + r_{i_k}^{\mathrm{DL}}[k] \\
&= \omega_{\mathrm{BS}}(W_{\mathrm{RF}}^{\mathrm{DL},i_k})^H H_{i_k,b_i}^{\mathrm{DL}}[k] F_{\mathrm{RF}}^{\mathrm{BS},b} s_{b_i}^{\mathrm{BS}}[k] + \tilde{n}_{i_k}^{\mathrm{DL}}[k]
\end{aligned} \tag{6}$$

where $H_{i_k,b}^{\mathrm{DL}}[k]$ is the DL channel coefficients matrix at the k^{th} subcarrier from BS b to the DL user i_k, $H_{i_k,j_k}^{\mathrm{DU}}[k]$ is the channel coefficients matrix from UL user j_k to DL user i_k, $n_i^{\mathrm{DL}}[k]$ is

the AWGN at DL user i_k that $n_i^{\mathrm{DL}}[k] \sim \mathcal{CN}\left(\mathbf{0}, \sigma_{\mathrm{UE}}^2 \mathbf{I}_{M_{\mathrm{RF}}^{\mathrm{Rx}}}\right)$, $\widetilde{n}_{i_k}^{\mathrm{DL}}[k]$ represents all the interference and noise terms, and $r_{i_k}^{\mathrm{DL}}[k]$ represents the receiver distortion at the DL user i_k, which can also be described by Equation (5). It should be noted that the quantisation noise is not specially described here since the received signals at UEs are usually within the dynamic range of ADCs, so its effect is included in $r_{i_k}^{\mathrm{DL}}[k]$. The intended signal for DL user i_k is transmitted by BS b_i, i.e., the first term on the right hand side is the signal of interest.

C. QUANTISATION NOISE

Let $\bar{\mathbf{y}}_g^{\mathrm{BS}}[k] = \mathbf{y}_g^{\mathrm{BS}}[k] - \mathbf{n}_g^{\mathrm{qtz}}[k]$ denote input signals of ADCs at these RF chains, the quantisation noise can be described by the Gaussian model as [19]

$$\mathbf{n}_g^{\mathrm{qtz}}[k] \sim \mathcal{CN}\left(\mathbf{0}, \rho(1-\rho) \cdot \mathcal{D}\left(\bar{\mathbf{y}}_g^{\mathrm{BS}}[k]\left(\bar{\mathbf{y}}_g^{\mathrm{BS}}[k]\right)^H\right)\right) \quad (7)$$

where $\rho = \frac{\pi\sqrt{3}}{2} \cdot 2^{-2b}$ if $b > 5$, for the case $b \leq 5$, the value of ρ can be found in Table 1 in [19].

D. FR2 CHANNEL MODEL

Let $\mathbf{H}(\tau)$ denote the time-domain channel matrix between the transmit and receive antenna arrays. Each element of $\mathbf{H}(\tau)$ at delay τ consists of line of sight (LOS) and non line of sight (NLOS) components and is given as [20]

$$[\mathbf{H}]_{r,s}(\tau) = \sqrt{\frac{K}{(1+K)}} h_{rs}^{\mathrm{LOS}} + \sqrt{\frac{1}{(K+1)}} \sum_{n=1}^{L} \sum_{m_n=1}^{M_n} h_{rs,n,m_n}^{\mathrm{NLOS}}(\tau - \tau_n - \tau_{m_n}) \quad (8)$$

where r and s represent the r^{th} receive and s^{th} transmit antenna respectively, L is the number of clusters, M_n is the number of rays in n^{th} cluster, τ_n is the delay of the n^{th} cluster, τ_{m_n} is the delay of m_n^{th} ray in the n^{th} cluster, and K is the Rician factor. h_{rs}^{LOS} and $h_{rs,n,m_n}^{\mathrm{NLOS}}$ denote the complex channel gains for LOS and NLOS paths given as

$$h_{rs}^{\mathrm{LOS}} = \begin{bmatrix} F_{\theta,\mathrm{GCS},r}(\theta_{\mathrm{LOS}}^A, \phi_{\mathrm{LOS}}^A) \\ F_{\phi,\mathrm{GCS},r}(\theta_{\mathrm{LOS}}^A, \phi_{\mathrm{LOS}}^A) \end{bmatrix}^T \begin{bmatrix} F_{\theta,\mathrm{GCS},s}(\theta_{\mathrm{LOS}}^D, \phi_{\mathrm{LOS}}^D) \\ F_{\phi,\mathrm{GCS},s}(\theta_{\mathrm{LOS}}^D, \phi_{\mathrm{LOS}}^D) \end{bmatrix} \times e^{j\frac{2\pi}{\lambda}\left(e_r(\theta_{\mathrm{LOS}}^A, \phi_{\mathrm{LOS}}^A)^T d_r\right)} \cdot e^{j\frac{2\pi}{\lambda}\left(e_r(\theta_{\mathrm{LOS}}^D, \phi_{\mathrm{LOS}}^D)^T d_s\right)} \quad (9)$$

$$h_{rs,n,m_n}^{\mathrm{NLOS}} = \begin{bmatrix} F_{\theta,\mathrm{GCS},r}(\theta_{n,m_n}^A, \phi_{n,m_n}^A) \\ F_{\phi,\mathrm{GCS},r}(\theta_{n,m_n}^A, \phi_{n,m_n}^A) \end{bmatrix}^T \begin{bmatrix} F_{\theta,\mathrm{GCS},s}(\theta_{n,m_n}^D, \phi_{n,m_n}^D) \\ F_{\phi,\mathrm{GCS},s}(\theta_{n,m_n}^D, \phi_{n,m_n}^D) \end{bmatrix} \times e^{j\frac{2\pi}{\lambda}\left(e_r(\theta_{n,m_n}^A, \phi_{n,m_n}^A)^T d_r\right)} \cdot e^{j\frac{2\pi}{\lambda}\left(e_r(\theta_{n,m_n}^D, \phi_{n,m_n}^D)^T d_s\right)} \quad (10)$$

where $F_{\theta,\mathrm{GCS},r}$, $F_{\phi,\mathrm{GCS},r}$, $F_{\theta,\mathrm{GCS},s}$, and $F_{\phi,\mathrm{GCS},s}$ are the radiation field patterns in the direction of the spherical basis vectors e_θ and e_ϕ of the s^{th} transmit antenna and r^{th} receive antenna, respectively. θ^A and ϕ^A represent the elevation and azimuth angle of arrival (AoA) for associated LOS path or the m_n^{th} NLOS ray in n^{th} cluster respectively, and θ^D and ϕ^D represent the elevation and azimuth angle of departure (AoD) for associated LOS path or the m_n^{th} NLOS ray in n^{th} cluster respectively. d_r and d_s are the position vectors of the receive antenna r and transmit antenna s given in the global coordinate system (GCS) respectively. λ denotes the wavelength of the carrier frequency. Specifically, the NLOS component of SI channels is the same as given in Equations (8) and (10), while the complex gain of the LOS component of SI channels is given as [21]

$$h_{rs}^{\mathrm{LOS,SI}} = \begin{bmatrix} F_{\theta,\mathrm{GCS},r}(\theta_{\mathrm{LOS}}^A, \phi_{\mathrm{LOS}}^A) \\ F_{\phi,\mathrm{GCS},r}(\theta_{\mathrm{LOS}}^A, \phi_{\mathrm{LOS}}^A) \end{bmatrix}^T \begin{bmatrix} F_{\theta,\mathrm{GCS},s}(\theta_{\mathrm{LOS}}^D, \phi_{\mathrm{LOS}}^D) \\ F_{\phi,\mathrm{GCS},s}(\theta_{\mathrm{LOS}}^D, \phi_{\mathrm{LOS}}^D) \end{bmatrix} \times \frac{1}{d_{rs}} e^{-j2\pi\frac{d_{rs}}{\lambda}} \quad (11)$$

where d_{rs} is the distance between the s^{th} transmit antenna and r^{th} receive antenna.

E. END-TO-END LATENCY

The total end-to-end latency can be described as [3], [22]

$$T_{\mathrm{total}} = T_{\mathrm{ttt}} + T_{\mathrm{ppg}} + T_{\mathrm{buff}} + T_{\mathrm{pcs}} \quad (12)$$

- T_{ttt} is the time-to-transmit latency.
- T_{ppg} is the propagation latency determined by the signal travel distance.
- T_{buff} is the buffering latency associated with receiving the signal at the receiver.
- T_{pcs} is the processing latency that the transceiver encodes and decodes the signal and estimates the channel, etc.

T_{pcs} can be reduced by self-contained sub-frames and new physical layer design as in [3], while T_{ppg} is determined only by the travel distance and is small. We focus on reducing T_{ttt} and T_{buff}, which depend on the slot length and can be reduced by advanced frame structures inspired by IBFD radios, 5G NR numerology and mini-slot supported by FR2 band.

IBFD radios allow UL eMBB devices and DL URLLC devices to use any time slot and subcarrier simultaneously. So there is no need to reserve time slots for URLLC devices as in TDD systems and double the number of available subcarriers than FDD systems. FR2 band provides enormous frequency resources for signalling, redundancy, and parity to provide ultra-low latency with high reliability. 5G NR introduces multiple types of numerology, i.e., 15 kHz, 30 kHz, 60 kHz, 120 kHz, and 240 kHz of subcarrier spacing, to reduce the symbol duration time [23]. For instance, expanding the subcarrier spacing from 15 kHz to 60 kHz can reduce the symbol duration time from 72 μs to 18 μs. Utilising FR2 band, we have to reduce the cell radius and densely deploy base stations due to the high path loss. Thus, the channel delay spread will be smaller than FR1 band channels. This indicates that FR2 band can support higher numerology. It should be noted that there can still be a large number of subcarriers with expanded subcarrier spacing to deliver high throughput in FR2 due to the ultra-wide bandwidth provided by FR2 spectrum. To reduce the

processing latency, we put all the reference and control signals, e.g., physical data shared channel-demodulation reference signal (PDSCH-DMRS), at the first few symbols of the 14 symbols in a slot, known as self-contained sub-frames. Thus, the PDSCH-DMRS have been decoded and the channel estimation has been done when the DL payload is received, and the receiver can start decoding the DL payload immediately. Besides, mini-slot (e.g., 7 symbols in a slot) is specially introduced to be a remedy of latency reduction for URLLC at the cost of achievable rate reduction due to the fact that URLLC service usually does not require a huge data throughput [3]. With all these technologies, the slot length for URLLC devices can be reduced to 125 μs, i.e., $T_{\text{ttt}} = 125$ μs and $T_{\text{buff}} \leq 125$ μs, resulting the end-to-end latency $T_{\text{total}} \leq 0.5$ ms with the propagation and processing latencies, and later simulation results in Section V demonstrate $\geq$ 99.999% reliability can be achieved with such low latency.

III. SIGNAL PROCESSING FOR FULL-DUPLEX

IBFD introduces significant self-interference, which could be 100 dB higher than the received signal of interest (SoI) due to the proximity of the transmit and receive antenna arrays at the IBFD base station [24]. Thus, it has to be efficiently suppressed; otherwise, the SoI will be swamped, and the UL communications will be invalidated [4], [18]. Typically, the significant SI is suppressed through three steps, where antenna isolation and active RF cancellation are essential to prevent the receiver from saturation [8] and digital cancellation processes the residual self-interference (RSI) due to imperfect analog cancellation. In this section, we propose active signal processing methods in the analog and digital domain (i.e., RF and digital cancellation) to efficiently suppress the SI over a wide band with low latency. In contrast, the CCI will experience natural propagation loss and will not exceed the receiver dynamic range. In this section, we propose a user allocation policy to minimise the CCI in the propagation domain, so it can be efficiently managed through appropriate digital beamforming, such as the weighted sum rate beamforming in [7].

A. ANTENNA ISOLATION

There are usually three passive antenna isolation methods, i.e., spatial separation, non-reciprocity of circulators, and antenna polarisations for single-input and single-output (SISO) cases. These basic techniques provide about 10-20 dB of isolation level, while it can be improved to 30 dB with the help of further decoupling network or reflection control circuit [25]. All three methods can be combined for antenna arrays, but only the spatial separation method can be used multiple times. It should be noted that the spatial separation method is not bandwidth limited, while the decoupling network and the reflection control circuit are bandwidth limited [25]. So, we consider a combination of spatial separation and non-reciprocity of circulators without decoupling networks or reflection control circuits for our design throughout this paper, offering a total of 15 dB of passive cancellation. This can be viewed as additional path loss of the SI channel without loss of generality, i.e., the complex gains of SI channel described as Equation (10) and (11) are reduced by 15 dB.

B. RF CANCELLATION

Typically, there are Stanford architecture and Rice architecture for RF cancellation [26]. The Stanford architecture taps the reference signal at transmitting antennas so that the reference signal contains the transmitter nonlinearity and distortions. It leads the RF canceller to only mimic the linear wireless SI channel. However, there are two limiting factors to extending such architecture to FR2 band:

- The first one is the operational bandwidth, which is usually limited by the insertion loss and poor frequency flatness of RF components utilised to construct the canceller [10].
- The second one is the huge number of required cancellers to match the antenna pairs with large-scale antenna array, i.e., $N_{\text{ant}}^{\text{TX}} \times N_{\text{ant}}^{\text{RX}}$ cancellers are required for the IBFD base station. Such a number is physically prohibitive with large-scale antenna arrays.

To address these issues, we propose a novel RF cancellation scheme, which explores optical components to break the bandwidth limitation due to hardware imperfections and takes advantage of the RF beamforming to reduce the number of required cancellers. Compared with previous studies, this design avoids using auxiliary transmitters and complex digital signal pre-processing as in [27] and can enlarge the operational bandwidth, which is difficult in RF domain [28].

We tap the reference signal from each transmitter RF chain and insert the nulling signal, which is generated by an optical domain-based canceller as Fig. 3, into the associated receiver RF chain instead of TX and RX antennas as Fig. 2 shows. It should be noted that although the hybrid beamforming architecture is commonly used in FR2 band communications, taking advantage of such architecture for feasible RF cancellation is still rare and valuable. By doing this, the number of required cancellers reduces from $N_{\text{ant}}^{\text{Tx}} \times N_{\text{ant}}^{\text{Rx}}$ to $N_{\text{RF}}^{\text{Tx}} \times N_{\text{RF}}^{\text{Rx}}$, which is a significant gain since $N_{\text{RF}}^{\text{Tx}} \ll N_{\text{ant}}^{\text{Tx}}$ and $N_{\text{RF}}^{\text{Rx}} \ll N_{\text{ant}}^{\text{Rx}}$, e.g., from 256×256 to 4×4. However, such an operation also changes the characteristics of the SI channel that the canceller needs to mimic. Conventionally, the canceller between a specific TX and RX antennas pair mimics the linear wireless SI channel between the two antennas, which can be described by the tapped delay line (TDL) model. In our design, we have to consider the effects of RF beamforming. Focus on a specific transmitter and receiver RF chains pair, e.g., the u^{th} transmitter RF chain and the v^{th} receiver RF chain, the output RF signal of the u^{th} transmitter RF chain is $x_u(t)$, then the v^{th} receiver RF chain receives signal caused by this transmitter RF chain as

$$y_v(t) = \sum_{j=1}^{N_{\text{ant},v}} a_j(t) \sum_{i=1}^{N_{\text{ant},u}} h_{ij}(t) * (a_i(t) x_u(t)) \tag{13}$$

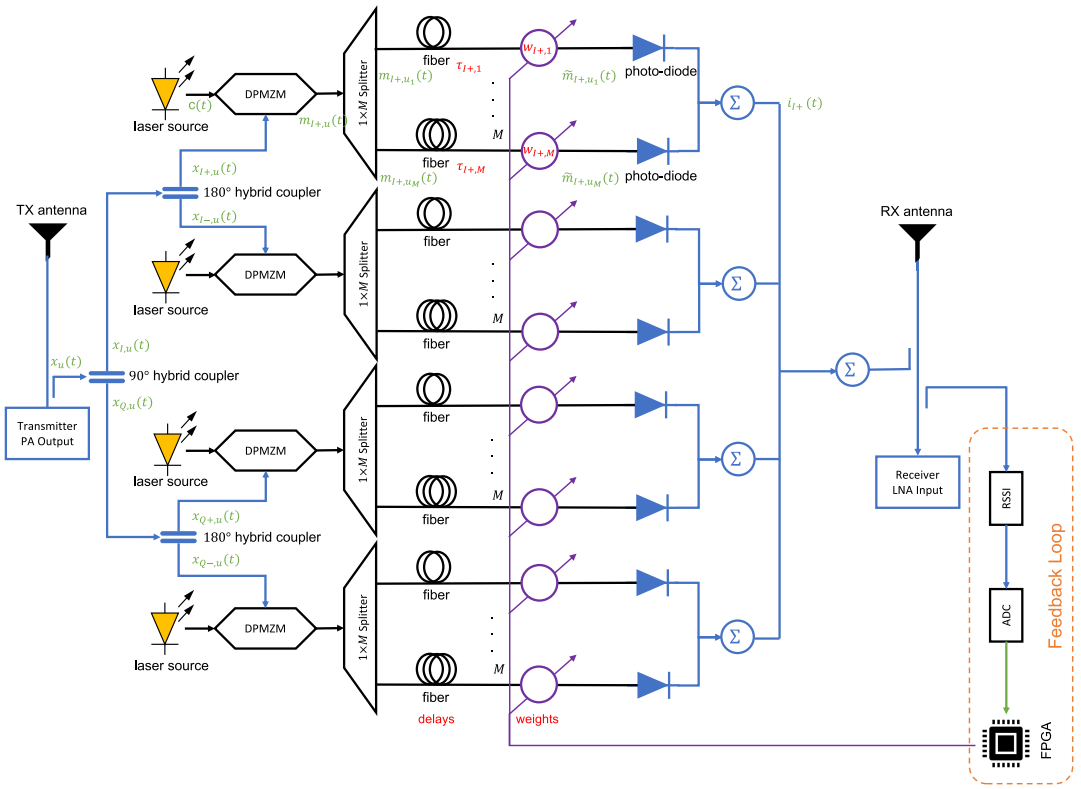

FIGURE 3. A block diagram demonstrates the signal processing of the proposed RF canceller.

where $N_{\text{ant},u}$ and $N_{\text{ant},v}$ denote the number of transmit and receive antennas connected to the u^{th} transmitter RF chain and v^{th} receiver RF chain, $a_i(t)$ and $a_j(t)$ are the complex coefficient introduced by the time-variant frequency-flat RF precoder and combiner at the i^{th} transmit antenna and j^{th} receive antenna, respectively, and $h_{ij}(t)$ is the wireless channel between the two antennas described by Equation (8) and can be denoted in an alternative way as

$$h_{ij}(t) = \alpha_{ij,0}(t)\delta(t - t_{ij,0}) + \sum_{l=1}^{L_{ij}} \alpha_{ij,l}(t)\delta(t - t_{ij,l}) \quad (14)$$

where $\alpha_{ij}(t)$ and t_{ij} are the channel coefficient and delay of associated path (e.g., $\alpha_{ij,l} = \sqrt{\frac{1}{K+1}} h^{\text{NLOS}}_{rs,n,m_n}$ and $t_{ij,l} = \tau_n + \tau_{m_n}$ if $l = n \cdot m_n$), $L_{ij} = L \cdot M_n$. Then, we can rewrite Equation (13) as

$$\begin{aligned} y_v(t) &= \sum_{j=1}^{N_{\text{ant},v}} \sum_{i=1}^{N_{\text{ant},u}} a_j(t) a_i(t) h_{ij}(t) * x_u(t) \\ &= \sum_{j=1}^{N_{\text{ant},v}} \sum_{i=1}^{N_{\text{ant},u}} a_j(t) a_i(t) h_{ij}(t) * x_u(t) \\ &= \left(\sum_{j=1}^{N_{\text{ant},v}} \sum_{i=1}^{N_{\text{ant},u}} \sum_{l=0}^{L_{ij}} a_j(t) a_i(t) \alpha_{ij,l}(t) \delta(t - t_{ij,l}) \right) \\ &\quad * x_u(t) \\ &= h_{\text{eff}}(t) * x_u(t) \end{aligned} \quad (15)$$

To suppress the SI from the u^{th} transmitter RF chain at the v^{th} receiver RF chain, we insert a canceller between the two RF chains to generate a nulling signal as $\widehat{y}_v(t) = h_{\text{canc}}(t) * x_u(t) = -h_{\text{eff}}(t) * x_u(t)$, where $h_{\text{eff}}(t) = \sum_{j=1}^{N_{\text{ant},v}} \sum_{i=1}^{N_{\text{ant},u}} \sum_{l=0}^{L_{ij}} a_j(t) a_i(t) \alpha_{ij,l}(t) \delta(t - t_{ij,l})$. First, we tap the output RF signal $x_u(t)$ via a 90° hybrid coupler with coupling factor α_1, which equally splits the RF reference signal with a resultant 90° phase shift between two output ports as

$$\begin{cases} x_{\text{I},u}(t) = \sqrt{\frac{1}{2}\alpha_1} e^{0j\pi} \cdot x_u(t) = \sqrt{\frac{1}{2}\alpha_1} \cdot x_u(t) \\ x_{\text{Q},u}(t) = \sqrt{\frac{1}{2}\alpha_1} e^{j\pi/2} \cdot x_u(t) = j\sqrt{\frac{1}{2}\alpha_1} \cdot x_u(t) \end{cases} \quad (16)$$

so the top two branches represent the I-channel, and the bottom two branches represent the Q-channel. Then we equally split the two signals via a 180° hybrid coupler with coupling factor α_2, which introduces 180° phase shift between two output ports as

$$\begin{cases} x_{\text{I+},u}(t) = \sqrt{\frac{1}{2}\alpha_2} e^{0j\pi} \cdot x_{\text{I},u}(t) = \frac{1}{2}\alpha_1\alpha_2 \cdot x_u(t) \\ x_{\text{I-},u}(t) = \sqrt{\frac{1}{2}\alpha_2} e^{j\pi} \cdot x_{\text{I},u}(t) = -\frac{1}{2}\alpha_1\alpha_2 \cdot x_u(t) \\ x_{\text{Q+},u}(t) = \sqrt{\frac{1}{2}\alpha_2} e^{0j\pi} \cdot x_{\text{Q},u}(t) = \frac{j}{2}\alpha_1\alpha_2 \cdot x_u(t) \\ x_{\text{Q-},u}(t) = \sqrt{\frac{1}{2}\alpha_2} e^{j\pi} \cdot x_{\text{Q},u}(t) = -\frac{j}{2}\alpha_1\alpha_2 \cdot x_u(t) \end{cases} \quad (17)$$

Then the phase-shifted reference signals are converted into the optical domain through intensity modulation by the

dual-parallel Mach-Zehnder modulator (DPMZM). The laser source generates the carrier with frequency f_c and amplitude A_c such that $c(t) = A_c \cdot \cos(2\pi f_c t)$. The modulated optical signal can be given as

$$\begin{aligned} m_{\text{I+},u}(t) &= l_{\text{MZM}} A_c \left(1 + x_{\text{I+},u}(t)\right) \cos(2\pi f_c t) \\ &= l_{\text{MZM}} A_c \left(1 + \frac{1}{2}\alpha_1\alpha_2 \cdot x_u(t)\right) \cos(2\pi f_c t) \end{aligned} \tag{18}$$

where l_{MZM} is the insertion loss of the DPMZM. We only model the I+ branch since other 3 branches have identical architecture and can be similarly described, e.g., $m_{\text{Q-},u}(t) = l_{\text{MZM}} A_c \left(1 - \frac{j}{2}\alpha_1\alpha_2 \cdot x_u(t)\right) \cos(2\pi f_c t)$. The modulated optical signal will be equally splitted by the splitter, and each output port of the splitter can be described as

$$\begin{aligned} m_{\text{I+},u_m}(t) &= \sqrt{\frac{1}{M}} l_{\text{sp}} \cdot m_{\text{I+},u}(t) \\ &= \sqrt{\frac{1}{M}} l_{\text{sp}} l_{\text{MZM}} A_c \left(1 + \frac{1}{2}\alpha_1\alpha_2 \cdot x_u(t)\right) \cos(2\pi f_c t) \end{aligned} \tag{19}$$

where l_{sp} is the insertion loss of the splitter. Then these signals are propagated into different-length independent fiber associated with VOAs and photo-diodes, which we call a fiber array. These signals will be delayed due to the natural propagation delay and be weighted by the VOA, which can be described as

$$\begin{aligned} \widetilde{m}_{\text{I+},u_m}(t) &= l_{\text{fb}}(m) l_{\text{VOA}} \cdot w_{\text{I+},m} m_{\text{I+},u_m}(t - t_{\text{I+},m}) \\ &= l_{\text{IL}} l_{\text{fb}}(m) w_{\text{I+},m} A_c \left(1 + \frac{1}{2}\alpha_0 \cdot x_u(t - t_{\text{I+},m})\right) \\ &\quad \cdot \cos(2\pi f_c (t - t_m)) \end{aligned} \tag{20}$$

where $l_{\text{fb}}(m)$ is the propagation loss and t_m is the propagation delay, which are determined by the fiber length of corresponding tap m, $l_{\text{IL}} = \sqrt{\frac{1}{M}} l_{\text{VOA}} l_{\text{sp}} l_{\text{MZM}}$ describes the fix hardware insertion loss, and $\alpha_0 = \alpha_1\alpha_2$ captures the total coupling factor. Finally, these signals are converted back by photo-diodes through direct detection and combined together to form the output as

$$i_{\text{I+}}(t) = R_{\text{pd}} \sum_{m=1}^{M} \frac{\alpha_0 \left(l_{\text{IL}} l_{\text{fb}}(m) w_{\text{I+},m} A_c\right)^2}{2} x_u(t - t_{\text{I+},m}) \tag{21}$$

where R_{pd} is the responsivity of the photo-diode. This suggests that we get an accumulation of multiple phase-shifted, delayed and weighted versions of the input reference signal $x_u(t)$ at the output of each branch. In practice, hardware imperfections will introduce amplitude and phase imbalance to the four branches. So we use different subscripts to capture the practical insertionlosses and phase shifting of corresponding branches, and the canceller can be described as

$$\begin{aligned} h_{\text{canc}}(t) = &\sum_{m=1}^{M} \beta_{\text{I+},m} w_{\text{I+},m}^2 \delta(t - t_{\text{I+},m}) e^{j\phi_{\text{I+}}} \\ &+ \sum_{m=1}^{M} \beta_{\text{I-},m} w_{\text{I-},m}^2 \delta(t - t_{\text{I-},m}) e^{j\phi_{\text{I-}}} \\ &+ \sum_{m=1}^{M} \beta_{\text{Q+},m} w_{\text{Q+},m}^2 \delta(t - t_{\text{Q+},m}) e^{j\phi_{\text{Q+}}} \\ &+ \sum_{m=1}^{M} \beta_{\text{Q-},m} w_{\text{Q-},m}^2 \delta(t - t_{\text{Q-},m}) e^{j\phi_{\text{Q-}}} \end{aligned} \tag{22}$$

where $\beta_m = \frac{\alpha_0 R_{\text{pd}} (l_{\text{IL}} l_{\text{fb}}(m) A_c)^2}{2}$. As explained in, designing the canceller in the time domain will loss the adaptability to environmental changes, so we convert it to the frequency domain via Fourier transformation as

$$\begin{aligned} H_{\text{canc}}(\omega) = &\sum_{m=1}^{M} \beta_{\text{I+},m} w_{\text{I+},m}^2 e^{j(\phi_{\text{I+}} - \omega t_{\text{I+},m})} \\ &+ \sum_{m=1}^{M} \beta_{\text{I+},m} w_{\text{I+},m}^2 e^{j(\phi_{\text{I-}} - \omega t_{\text{I-},m})} \\ &+ \sum_{m=1}^{M} \beta_{\text{I+},m} w_{\text{I+},m}^2 e^{j(\phi_{\text{Q+}} - \omega t_{\text{Q+},m})} \\ &+ \sum_{m=1}^{M} \beta_{\text{I+},m} w_{\text{I+},m}^2 e^{j(\phi_{\text{Q-}} - \omega t_{\text{Q-},m})} = \mathbf{L}_\omega \mathbf{W} \end{aligned} \tag{23}$$

where $\mathbf{L}_\omega = \left[\mathbf{L}_{\text{I+},\omega}\ \mathbf{L}_{\text{I-},\omega}\ \mathbf{L}_{\text{Q+},\omega}\ \mathbf{L}_{\text{Q-},\omega}\right]$, $\mathbf{W} = [\mathbf{W}_{\text{I+}}^T\ \mathbf{W}_{\text{I-}}^T\ \mathbf{W}_{\text{Q+}}^T\ \mathbf{W}_{\text{Q-}}^T]^T$, $\mathbf{L}_{p,\omega} = \left[\beta_{\text{I+},1} e^{j(\phi_{\text{I+}} - \omega t_{p,1})} \beta_{\text{I+},2} e^{j(\phi_{\text{I+}} - \omega t_{p,2})} \ \dots\ \beta_{\text{I+},M} e^{j(\phi_{\text{I+}} - \omega t_{p,M})}\right]$, $\mathbf{W}_p = [w_{p,1}^2 w_{p,2}^2 \dots\ w_{p,M}^2]^T$, and p is the placeholder for associated branch. The target of RF cancellation is to tune the canceller to be as close to the inverse effective SI channel as possible within the band of interest, which can be described as

$$\min_{\mathbf{W}} \int_{\omega_0}^{\omega_s} |H_{\text{canc}}(\omega) + H_{\text{eff}}(\omega)|^2 \, d\omega \tag{24}$$

$$s.t.\ 0 \le [\mathbf{W}]_{x,1} \le 1 \tag{25}$$

where the constraints come from passive VOAs to minimise the canceller's nonlinearity. Assume the effective SI channel can be well characterised by $K_s + 1$ samples within the band of interest $[\omega_0, \omega_s]$ (e.g., [27.8 GHz, 28.2 GHz]), where sampling interval $\Delta_\omega = \frac{\omega_s - \omega_0}{K_s}$, so $\mathbf{H}_{\text{eff}} = \left[H_{\text{eff}}(\omega_0)\ H_{\text{eff}}(\omega_1)\ \dots\ H_{\text{eff}}(\omega_{K_s})\right]^T$ can accurately describe the effective SI channel within the band of interest, and the canceller at corresponding frequency components can be denoted as

$$\mathbf{H}_{\text{canc}} = \left[\mathbf{L}_{\omega_0}^T\ \mathbf{L}_{\omega_1}^T\ \dots\ \mathbf{L}_{\omega_{K_s}}^T\right]^T \mathbf{W} = \mathbf{L}\mathbf{W} \tag{26}$$

Then, we can derive the optimal solution of the tuneable weights according to the minimum mean-square error (MMSE) criterion as

$$\mathbf{W}^{*}_{\mathrm{MMSE}} = -\left(\mathbf{L}^{H}\mathbf{L}\right)^{-1}\mathbf{L}^{H}\mathbf{H}_{\mathrm{eff}} \tag{27}$$

It should be noted that the $\mathbf{W}^{*}_{\mathrm{MMSE}}$ gives the optimal performance that can be achieved with M taps (i.e., M tuneable variables).

1) PRACTICAL IMPLEMENTATION

The fiber length depends on the access delay spread of the effective RF SI channel between specific RF chain pair, e.g., between the v^{th} receiver RF chain and the u^{th} transmitter RF chain. Assume $\tau^{\mathrm{NLOS}}_{vu,max}$ is the maximum delay of the significant NLOS paths (above the noise floor) and τ^{LOS}_{vu} denotes the delay of the LOS path, then the access delay spread of this channel is $\tau^{\mathrm{access}}_{vu} = \tau^{\mathrm{NLOS}}_{vu,max} - \tau^{\mathrm{LOS}}_{vu}$ and the length of the m^{th} fiber is

$$L_{vu,m} = \tau^{\mathrm{LOS}}_{vu}\cdot c + \frac{\tau^{\mathrm{access}}_{vu}\cdot c(m-1)}{M-1} \tag{28}$$

where c is the light speed. This makes the propagation delays of the M taps uniformly distributed within the delay spread of the effective SI channel, such that $\tau_{vu,m} = \tau^{\mathrm{LOS}}_{vu} + \tau^{\mathrm{access}}_{vu}\frac{m-1}{M-1}$. As for tuning the weights, we can have the matrix $\mathbf{L}$ in Equation (27) once the canceller is built, while $\mathbf{H}_{\mathrm{eff}}$ is usually unviable since the channel estimation happens after the RF cancellation stage. However, if the statistics of the effective SI channel can be explored, this problem can still be solved by the common Wiener solution as in [8] or the gradient descent search algorithm with the residual signal strength indicator as in [29].

2) CANCELLER NONLINEARITY & NOISE

In addition to the desired nulling signal, the canceller will also introduce additional noise and nonlinear distortions. The noise consists of the AWGN introduced by laser sources and the shot noise from photo-diodes, while the nonlinearities come from the DPMZM and VOAs. The nonlinearity introduced by the modulation profile can be suppressed to the noise floor by filters and appropriate bias voltages of the DPMZM. These noises and nonlinearities can be described by the complex Gaussian model so that the SI term in the received signal model (i.e., $\omega_{\mathrm{BS}}\left(\mathbf{W}^{\mathrm{BS},g}_{\mathrm{RF}}\right)^{H} H_{\mathrm{SI},g}[k]\mathbf{F}^{\mathrm{BS},g}_{\mathrm{RF}}\left(s^{\mathrm{BS}}_{g}[k] + t^{\mathrm{BS}}_{g}[k]\right)$) becomes $\omega_{\mathrm{BS}}\left[\left(\mathbf{W}^{\mathrm{BS},g}_{\mathrm{RF}}\right)^{H} H_{\mathrm{SI},g}[k]\mathbf{F}^{\mathrm{BS},g}_{\mathrm{RF}} + C_{\mathrm{RF},g}[k]\right]\left(s^{\mathrm{BS}}_{g}[k] + t^{\mathrm{BS}}_{g}[k]\right) + n^{\mathrm{canc}}_{g}[k]$ after the RF cancellation, where each element of $C_{\mathrm{RF},g}[k]$ is obtained through sampling associated RF canceller at corresponding frequency, and

$$n^{\mathrm{canc}}_{g}[k] \sim \mathcal{CN}\left(\mathbf{0}, \sigma^{2}_{\mathrm{canc}}\mathbf{I}_{N^{\mathrm{Rx}}_{\mathrm{RF}}}\right) \tag{29}$$

where $\sigma^{2}_{\mathrm{canc}}$ captures the amount of in-band noise and nonlinearities introduced by the canceller.

3) KEY AFFECTING FACTORS

This canceller does not rely on specific SI channel conditions, although more complex channels call for more taps for efficient performance. The important SI channel parameters associated with RF cancellation are excess delay and root mean square (RMS) delay. The RMS delay determines the coherence bandwidth, i.e., frequency-selectivity, of the SI channel, so it affects the number of required taps. The excess delay determines the delays of the canceller's taps. The excess delay is the delay difference between the LOS path and the last significant NLOS path, while the RMS delay τ_{RMS} is the second moment of the power delay profile of the SI channel, which can be described as

$$\tau_{RMS} = \sqrt{\frac{\sum_{j=1}^{N_{\mathrm{ant},v}}\sum_{i=1}^{N_{\mathrm{ant},u}}\sum_{l=0}^{L_{ij}}\chi_{ij,l}t^{2}_{ij,l}}{\sum_{j=1}^{N_{\mathrm{ant},v}}\sum_{i=1}^{N_{\mathrm{ant},u}}\sum_{l=0}^{L_{ij}}\chi_{ij,l}} - \tau_{0}^{2}} \tag{30}$$

where $\chi_{ij,l} = \left|a_j\alpha_{ij,l}a_i\right|^2$ captures the power profile of associated rays and τ_0 represents the mean delay of the SI channel that can be described as

$$\tau_{0} = \frac{\sum_{j=1}^{N_{\mathrm{ant},v}}\sum_{i=1}^{N_{\mathrm{ant},u}}\sum_{l=0}^{L_{ij}}\chi_{ij,l}t_{ij,l}}{\sum_{j=1}^{N_{\mathrm{ant},v}}\sum_{i=1}^{N_{\mathrm{ant},u}}\sum_{l=0}^{L_{ij}}\chi_{ij,l}} \tag{31}$$

The RF beamformer reduces the number of paths between any two nodes since it leads the transmitted beam to a specific direction, but it will increase the RMS delay of the SI channel. This suggests that the coherence bandwidth of the effective SI channel is smaller than the wireless SI channel (i.e., without RF beamforming effects), so more taps are needed to well characterise the effective SI channel within a specific band. It is demonstrated that the insertion loss is the obstacle to creating sufficient taps [8]. The proposed design solves this problem from two aspects:

- Optical components have much smaller insertion and propagation losses than RF components;
- Improving the power of optical carriers can compensate for the insertion loss as Equation (22) suggests.

Thus, it can provide much more taps than conventional RF domain-based cancellers (e.g., up to 100 taps in theory).

Remark: It should be noted that the number of taps is mostly proportional to the operational bandwidth and delay spread of the SI channel for specific cancellation depths [8], but more taps created in the canceller results in more VOAs, photo-diodes, and fibers, which increases the area and financial cost of RF cancellers. This suggests that a trade-off between the implementation cost and the cancellation depth must be made; otherwise, we would like to create as many taps as possible to minimise the SI effects at the IBFD node. Furthermore, the noise and nonlinearities of cancellers can be reduced by more elaborate components, but also results in higher financial costs.

4) PERFORMANCE ANALYSIS

For a specific subcarrier, the RF cancellation performance can be described by the average cancellation depth of all

$N_{\mathrm{RF}}^{\mathrm{Rx}} \times N_{\mathrm{RF}}^{\mathrm{Tx}}$ cancellers as

$$\eta_g^{\mathrm{RF}} = \mathbb{E}\left\{D_{ij,g,k}^{\mathrm{RF}}\right\} = \frac{\sum_{k=1}^{K_c}\sum_{i=1}^{N_{\mathrm{RF}}^{\mathrm{Rx}}}\sum_{j=1}^{N_{\mathrm{RF}}^{\mathrm{Tx}}} D_{ij,g,k}^{\mathrm{RF}}}{K_c \times N_{\mathrm{RF}}^{\mathrm{Rx}} \times N_{\mathrm{RF}}^{\mathrm{Tx}}} \tag{32}$$

where $D_{ij,g,k}^{\mathrm{RF}} = \frac{\left|\left[\mathbf{H}_{\mathrm{SI},g}^{\mathrm{eff}}[k]\right]_{i,j}\right|^2}{\left|\left[\mathbf{H}_{\mathrm{RSI},g}^{\mathrm{eff}}[k]\right]_{i,j}\right|^2}$ describes the cancellation depth at subcarrier k of associated canceller, and K_c is the number of subcarriers. The statistics of the residual self-interference channel is given as $\mathbb{E}\left\{\mathbf{H}_{\mathrm{RSI},g}^{\mathrm{eff}}\left(\mathbf{H}_{\mathrm{RSI},g}^{\mathrm{eff}}\right)^H\right\} = \mathcal{D}\left(\varpi_1, \varpi_2, \ldots, \varpi_{N_{\mathrm{RF}}^{\mathrm{Rx}}}\right)$, where $\varpi_i = \frac{1}{\eta_g^{\mathrm{RF}}}\mathbb{E}\left\{\left[\mathbf{H}_{\mathrm{SI},g}^{\mathrm{eff}}\right]_{i,j}\left[\mathbf{H}_{\mathrm{SI},g}^{\mathrm{eff}}\right]_{i,j}^*\right\}$. So we have

$$\mathbb{E}\left\{\mathbf{H}_{\mathrm{RSI},g}^{\mathrm{eff}}\left(\mathbf{H}_{\mathrm{RSI},g}^{\mathrm{eff}}\right)^H\right\} = \frac{1}{\eta_g^{\mathrm{RF}}}\mathbb{E}\left\{\mathbf{H}_{\mathrm{SI},g}^{\mathrm{eff}}\left(\mathbf{H}_{\mathrm{SI},g}^{\mathrm{eff}}\right)^H\right\} \tag{33}$$

C. DIGITAL CANCELLATION

The digital cancellation also follows the subtractive idea that a nulling signal is generated with the knowledge of the transmit SI signal and the estimated channel state information (CSI) from pilot signals. Different from previous studies, which operate in the time domain [12], we operate in the frequency domain to reduce the processing latency in conjunction with the self-contained sub-frames as introduced above. The physical data shared channel-demodulation reference signal (PDSCH-DMRS) is used as the pilot signal at specified subcarrier index in the first N_t^{plt} OFDM symbols in a slot. After the analog SIC, the received SI can be digitised with trivial quantisation noise. The frequency-domain digital residual self-interference (RSI) signal at the pilot subcarrier k_p is given as:

$$\begin{aligned} y_{\mathrm{RSI}}^{\mathrm{BS},g}[k_p] &= H_{\mathrm{RSI},g}^{\mathrm{eff}}[k_p]\left(s_g^{\mathrm{BS}}[k_p] + t_g^{\mathrm{BS}}[k_p]\right) \\ &\quad + n_g^{\mathrm{canc}}[k_p] + n_g^{\mathrm{BS}}[k_p] + n_g^{\mathrm{qtz}}[k_p] + r_g^{\mathrm{BS}}[k_p] \\ &= H_{\mathrm{RSI},g}^{\mathrm{eff}}[k_p]s_g^{\mathrm{BS}}[k_p] + \tilde{n}_{\mathrm{RSI}}^{\mathrm{BS},g}[k_p] \end{aligned} \tag{34}$$

where $H_{\mathrm{RSI},g}^{\mathrm{eff}}[k_p] = \omega_{\mathrm{BS}}[(\mathbf{W}_{\mathrm{RF}}^{\mathrm{BS},g})^H H_{\mathrm{SI},g}[k_p]\mathbf{F}_{\mathrm{RF}}^{\mathrm{BS},g} + C_{\mathrm{RF},g}[k_p]]$ represents the effective RSI channel coefficients at the k_p^{th} subcarrier that includes the effects of RF precoder, RF combiner, and RF cancellers at the k_p^{th} subcarrier, and $\tilde{n}_{\mathrm{RSI}}^{\mathrm{BS},g}[k_p]$ represents all residual terms except the received SI. Interference from other nodes are not present here since an interference-free period is usually provided by the MAC protocol via carrier sense to achieve accurate channel estimation. The estimated channel coefficients at pilot subcarrier k_p is given as:

$$\widehat{H}_{\mathrm{RSI},g}^{\mathrm{eff}}[k_p] = y_{\mathrm{RSI}}^{\mathrm{BS},g}[k_p]\left((s_g^{\mathrm{BS}}[k_p])^H s_g^{\mathrm{BS}}[k_p]\right)^{-1}(s_g^{\mathrm{BS}}[k_p])^H \tag{35}$$

The channel coefficients at the remaining subcarriers are calculated by interpolation on the estimated channel coefficients at pilot subcarriers $\{k_p\}_{p=1}^{N_f^{\mathrm{plt}}}$. The estimated channel coefficients matrix is valid for later symbols in the same slot since they are within the coherence time. With known $s_g^{\mathrm{BS}}[k]$, the RSI can be reconstructed as

$$\widehat{y}_{\mathrm{RSI},g}^{\mathrm{FD}}[k] = \widehat{H}_{\mathrm{RSI},g}^{\mathrm{eff}}[k]s_g^{\mathrm{BS}}[k] \tag{36}$$

Then, the RSI can be subtracted from the received signal and the intended UL payload can be decoded with only self-interference effects coming from imperfect channel estimation.

1) COMPLEXITY

The effective channel coefficients are estimated through the PDSCH-DMRS pilot signal at the initial N_t^{plt} symbols within a slot. Assume the pilot signal is inserted into N_f^{plt} subcarriers at the first symbols, the total coefficients need to be estimated, i.e., computational complexity, is given as $\mathcal{O}_{\mathrm{digital}}(N_f^{\mathrm{plt}} \times N_t^{\mathrm{plt}})$. This indicates the complexity of such digital canceller is not affected by the antenna array size as [12] does, so it is suitable for large antenna arrays.

2) PERFORMANCE ANALYSIS

The estimated and actual effective RSI channels at subcarrier k can be related as

$$H_{\mathrm{RSI},g}^{\mathrm{eff}}[k] = \widehat{H}_{\mathrm{RSI},g}^{\mathrm{eff}}[k] + \Delta_{\mathrm{eff},g}[k] \tag{37}$$

where $\Delta_{\mathrm{eff},g}[k] \sim \mathcal{CN}\left(\mathbf{0}, \varepsilon_g \mathbf{I}_{N_{\mathrm{RF}}^{\mathrm{Rx}}}\right)$, $\varepsilon_g = \frac{l_g^{\mathrm{SI}}}{\eta_g^{\mathrm{RF}}}\frac{\sigma_t^2+\sigma_r^2+\rho(1-\rho)}{(1+\sigma_t^2)}\frac{N_{\mathrm{ant}}^{\mathrm{Rx}}}{N_{\mathrm{sub}}^{\mathrm{Rx}}} + \frac{\sigma_{\mathrm{canc}}^2+\sigma_{\mathrm{BS}}^2}{P_{\mathrm{BS}}}$ as given in Appendix C. The digital SIC depth is given as

$$\begin{aligned} D_{g,k}^{\mathrm{dig}} &= \frac{\mathbb{E}\left\{tr\left(H_{\mathrm{RSI},g}^{\mathrm{eff}}[k]\left(H_{\mathrm{RSI},g}^{\mathrm{eff}}[k]\right)^H\right)\right\}}{\mathbb{E}\left\{tr\left(\Delta_{\mathrm{eff},g}[k]\left(\Delta_{\mathrm{eff},g}[k]\right)^H\right)\right\}} \\ &= \frac{\left(\frac{l_g^{\mathrm{SI}}}{\eta_g^{\mathrm{RF}}(1+\sigma_t^2)}\frac{N_{\mathrm{RF}}^{\mathrm{Tx}}N_{\mathrm{ant}}^{\mathrm{Rx}}}{N_{\mathrm{sub}}^{\mathrm{Rx}}}\right)\cdot N_{\mathrm{RF}}^{\mathrm{Rx}}}{\left(\frac{l_g^{\mathrm{SI}}}{\eta_g^{\mathrm{RF}}}\frac{\sigma_t^2+\sigma_r^2+\rho(1-\rho)}{(1+\sigma_t^2)}\frac{N_{\mathrm{ant}}^{\mathrm{Rx}}}{N_{\mathrm{sub}}^{\mathrm{Rx}}} + \frac{\sigma_{\mathrm{canc}}^2+\sigma_{\mathrm{BS}}^2}{P_{\mathrm{BS}}}\right)\cdot N_{\mathrm{RF}}^{\mathrm{Rx}}} \\ &= \frac{N_{\mathrm{RF}}^{\mathrm{Tx}}}{\sigma_t^2+\sigma_r^2+\rho(1-\rho)+\frac{\eta_g^{\mathrm{RF}}(1+\sigma_t^2)(\sigma_{\mathrm{canc}}^2+\sigma_{\mathrm{BS}}^2)N_{\mathrm{sub}}^{\mathrm{Rx}}}{P_{\mathrm{BS}}l_g^{\mathrm{SI}}N_{\mathrm{ant}}^{\mathrm{Rx}}}} \end{aligned} \tag{38}$$

which indicates the hybrid architecture, i.e., the number of transmitter RF chains and the number of subarrays at the receiver, will affect the digital cancellation performance. Besides, too deep RF cancellation (i.e., η_g^{RF} is large) will also degrade the digital cancellation performance. The degradation comes from the fact that the RF cancellation decreases the SNR of the SI signal for channel estimation in digital cancellation.

Remark: The advantage of our proposed frequency-domain based method is the significantly-reduced processing time to reduce the end-to-end latency, but the performance will be degraded if the nonlinearities of the transceiver or cancellers

are large as Equation (38) suggests. In contrast, there are polynomial cancellers [12] and neural network-based cancellers [13] that can deal with these nonlinear distortions and achieve deeper cancellation with larger processing latency. This means we have to make a trade-off between the cancellation depth and the latency and then decide which kind of digital canceller to use. Besides, Equation (38) also indicates that more RF chains and subarrays help with minimising SI effects while resulting in higher energy and financial cost. So we still need to make trade-offs between the cost and performance.

D. PERFORMANCE EVALUATION OF OVERALL SIC

1) NOISE FLOOR

We can describe the noise floor (include AWGN, transceiver distortions, canceller's noise and nonlinearities, and residual self-interference after digital cancellation) as

$$\begin{aligned}\Sigma^2_{\mathrm{SIF},g} &= \mathbb{E}\left\{\left(\Delta_{\mathrm{eff},g}\mathbf{s}_g^{\mathrm{BS}}+\tilde{n}_g^{\mathrm{BS}}\right)\left(\Delta_{\mathrm{eff},g}\mathbf{s}_g^{\mathrm{BS}}+\tilde{n}_g^{\mathrm{BS}}\right)^H\right\}\\ &= \frac{P_{\mathrm{BS}}}{N_{\mathrm{RF}}^{\mathrm{Tx}}}\varepsilon_g\mathbf{I}_{N_{\mathrm{RF}}^{\mathrm{Rx}}}+P_{\mathrm{BS}}\varepsilon_g\mathbf{I}_{N_{\mathrm{RF}}^{\mathrm{Rx}}}\\ &= \left(1+\frac{1}{N_{\mathrm{RF}}^{\mathrm{Tx}}}\right)P_{\mathrm{BS}}\varepsilon_g\mathbf{I}_{N_{\mathrm{RF}}^{\mathrm{Rx}}} \qquad (39)\end{aligned}$$

2) ACHIEVABLE UL RATE

After all stages of SIC applied, the received signal by BS g at the k^{th} subcarrier can be described as

$$\begin{aligned}&y^{\mathrm{BS}}_{g,\mathrm{SIF}}[k]\\ &= (W^{\mathrm{BS},g}_{\mathrm{RF}})^H H^{\mathrm{UL}}_{g,j_k}[k]F^{\mathrm{UL},j_k}_{\mathrm{RF}}\left(s^{\mathrm{UL}}_{j_k}[k]+t^{\mathrm{UL}}_{j_k}[k]\right)\\ &\quad+\Delta_{\mathrm{eff},g}s^{\mathrm{BS}}_g[k_p]+H^{\mathrm{eff}}_{\mathrm{RSI},g}[k]t^{\mathrm{BS}}_g[k]\end{aligned}$$

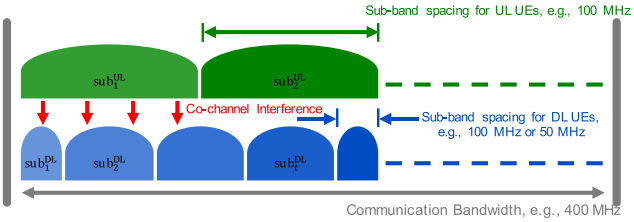

FIGURE 4. Orthogonal sub-bands division for UL and DL UEs.

$$\begin{aligned}&+\sum_{b\neq g}^{K_{\mathrm{BS}}}(W^{\mathrm{BS},g}_{\mathrm{RF}})^H H^{\mathrm{BS}}_{g,b}[k]F^{\mathrm{BS},b}_{\mathrm{RF}}\left(s^{\mathrm{BS}}_b[k]+t^{\mathrm{BS}}_b[k]\right)\\ &+n^{\mathrm{canc}}_g[k]+n^{\mathrm{BS}}_g[k]+n^{\mathrm{qtz}}_g[k]+r^{\mathrm{BS}}_g[k] \qquad (40)\end{aligned}$$

which yields the achievable rate of intended UL user j_k as

$$\begin{aligned}R^{\mathrm{UL}}_j &= \mathbb{E}\left\{\log_2\left(det\left(\mathbf{I}+\Theta_j[k]\Psi_j[k]^{-1}\right)\right)\right\}\\ &= \frac{1}{K_j}\sum_{k=1}^{K_j}\log_2\left(det\left(\mathbf{I}+\Theta_j[k]\Psi_j[k]^{-1}\right)\right) \qquad (41)\end{aligned}$$

where $\Theta_j[k]$ and $\Psi_j[k]$ are the signal power and interference-plus-noise power at subcarrier k given as Equations (42) and (43), as shown at the bottom of the page, and K_j is the number of indexes of subcarriers occupied by this user.

IV. SIGNAL PROCESSING FOR REDUCED CCI

IBFD radios also make DL users be interfered by UL users, which have overlapping frequency bands, which is known as co-channel interference. The CCI is not as strong as the SI to invalidate the communication due to the natural propagation

$$\begin{aligned}\Theta_j[k] &= cov\left((W^{\mathrm{BS},g}_{\mathrm{RF}})^H H^{\mathrm{UL}}_{g,j_k}[k]F^{\mathrm{UL},j_k}_{\mathrm{RF}}s^{\mathrm{UL}}_{j_k}[k]\right)\\ &= \mathbb{E}\left\{(W^{\mathrm{BS},g}_{\mathrm{RF}})^H H^{\mathrm{UL}}_{g,j_k}[k]F^{\mathrm{UL},j_k}_{\mathrm{RF}}s^{\mathrm{UL}}_{j_k}[k]\left((W^{\mathrm{BS},g}_{\mathrm{RF}})^H H^{\mathrm{UL}}_{g,j_k}[k]F^{\mathrm{UL},j_k}_{\mathrm{RF}}s^{\mathrm{UL}}_{j_k}[k]\right)^H\right\}\\ &= \frac{P_{\mathrm{UE},j}}{M^{\mathrm{Tx}}_{\mathrm{RF}}}(W^{\mathrm{BS},g}_{\mathrm{RF}})^H H^{\mathrm{UL}}_{g,j_k}[k]F^{\mathrm{UL},j_k}_{\mathrm{RF}}\left((W^{\mathrm{BS},g}_{\mathrm{RF}})^H H^{\mathrm{UL}}_{g,j_k}[k]F^{\mathrm{UL},j_k}_{\mathrm{RF}}\right)^H \qquad (42)\\ \Psi_j[k] &= cov\left(y^{\mathrm{BS}}_{g,\mathrm{SIF}}[k]-(W^{\mathrm{BS},g}_{\mathrm{RF}})^H H^{\mathrm{UL}}_{g,j_k}[k]F^{\mathrm{UL},j_k}_{\mathrm{RF}}s^{\mathrm{UL}}_{j_k}[k]\right)\\ &= (W^{\mathrm{BS},g}_{\mathrm{RF}})^H H^{\mathrm{UL}}_{g,j_k}[k]F^{\mathrm{UL},j_k}_{\mathrm{RF}}t^{\mathrm{UL}}_{j_k}[k]\left((W^{\mathrm{BS},g}_{\mathrm{RF}})^H H^{\mathrm{UL}}_{g,j_k}[k]F^{\mathrm{UL},j_k}_{\mathrm{RF}}t^{\mathrm{UL}}_{j_k}[k]\right)^H\\ &\quad+\frac{P_{\mathrm{BS}}}{N^{\mathrm{Tx}}_{\mathrm{RF}}}\Delta_{\mathrm{eff},g}\Delta^H_{\mathrm{eff},g}+H^{\mathrm{eff}}_{\mathrm{RSI},g}[k]t^{\mathrm{BS}}_g[k]\left(H^{\mathrm{eff}}_{\mathrm{RSI},g}[k]t^{\mathrm{BS}}_g[k]\right)^H\\ &\quad+\frac{P_{\mathrm{BS}}}{N^{\mathrm{Tx}}_{\mathrm{RF}}}\sum_{b\neq g}^{K_{\mathrm{BS}}}(W^{\mathrm{BS},g}_{\mathrm{RF}})^H H^{\mathrm{BS}}_{g,b}[k]F^{\mathrm{BS},b}_{\mathrm{RF}}\left((W^{\mathrm{BS},g}_{\mathrm{RF}})^H H^{\mathrm{BS}}_{g,b}[k]F^{\mathrm{BS},b}_{\mathrm{RF}}\right)^H\\ &\quad+\sum_{b\neq g}^{K_{\mathrm{BS}}}(W^{\mathrm{BS},g}_{\mathrm{RF}})^H H^{\mathrm{BS}}_{g,b}[k]F^{\mathrm{BS},b}_{\mathrm{RF}}t^{\mathrm{BS}}_b[k]\left((W^{\mathrm{BS},g}_{\mathrm{RF}})^H H^{\mathrm{BS}}_{g,b}[k]F^{\mathrm{BS},b}_{\mathrm{RF}}t^{\mathrm{BS}}_b[k]\right)^H\\ &\quad+n^{\mathrm{canc}}_g[k]\left(n^{\mathrm{canc}}_g[k]\right)^H+n^{\mathrm{BS}}_g[k]\left(n^{\mathrm{BS}}_g[k]\right)^H+n^{\mathrm{qtz}}_g[k]\left(n^{\mathrm{qtz}}_g[k]\right)^H+r^{\mathrm{BS}}_g[k]\left(r^{\mathrm{BS}}_g[k]\right)^H \qquad (43)\end{aligned}$$

loss but will still degrade the DL throughput. To combat the CCI and obtain the maximum IBFD gain, we propose a user allocation algorithm through a game-theoretic approach. Assume the whole communication bandwidth is separated into T_{DL} and T_{UL} orthogonal sub-bands for DL and UL users respectively as Fig. 4, where the sub-band can have different bandwidths to provide different performance profiles for a variety of user needs in IIoT networks. Let $\mathcal{X} = \{x^{\mathrm{DL}}, x^{\mathrm{UL}}\}$ denote user allocation policy which is the collections of all DL and UL indicators. x^{DL} and x^{UL} have dimension of $T_{\mathrm{DL}} \times K_{\mathrm{DL}}$ and $T_{\mathrm{UL}} \times K_{\mathrm{UL}}$ respectively. $[x^{\mathrm{DL}}]_{t_d,k_d} = 1$ if DL user k_d is allocated into the t_d^{th} DL sub-band $\mathrm{sub}_t^{\mathrm{DL}}$, and 0 otherwise. Similarly, $[x^{\mathrm{UL}}]_{t_u,k_u} = 1$ if UL user k_u is allocated into the t_u^{th} UL sub-band $\mathrm{sub}_t^{\mathrm{UL}}$, and 0 otherwise. There will be co-channel interference as long as the DL sub-bands and UL sub-bands overlap. The essence of user allocation is to allocate the DL and UL user pairs that may cause significant CCI to orthogonal sub-bands while leaving the user pairs with small CCI in the overlapping sub-bands. According to Equations (4) and (6), the achievable sum rate of DL user i and UL user j served by BS g can be described as

$$R_i^{\mathrm{DL}} = G_i^{\mathrm{DL}} \cdot \log_2\left(1 + \frac{M_{\mathrm{ant}}^{\mathrm{RX},i} P_i^{\mathrm{DL}} |h_{i,g}^{\mathrm{DL}}|^2}{\gamma_i^{\mathrm{DL}}}\right) \tag{44}$$

$$R_j^{\mathrm{UL}} = G_j^{\mathrm{UL}} \cdot \log_2\left(1 + \frac{N_{\mathrm{ant}}^{\mathrm{RX}} P_j^{\mathrm{UL}} |h_{g,j}^{\mathrm{UL}}|^2}{\gamma_j^{\mathrm{UL}}}\right) \tag{45}$$

where $G_i^{\mathrm{DL}} = \min\left\{M_{\mathrm{ant}}^{\mathrm{RX},i}, N_{\mathrm{ant}}^{\mathrm{TX}}\right\}$ and $G_j^{\mathrm{UL}} = \min\left\{N_{\mathrm{ant}}^{\mathrm{RX}}, M_{\mathrm{ant}}^{\mathrm{TX}}\right\}$ are the degrees of freedom gains for sum rate, γ_i^{DL} and γ_j^{UL} represent the power of interference plus noise for the i^{th} DL UE and j^{th} UL UE given as

$$\begin{aligned}\gamma_i^{\mathrm{DL}} &= M_{\mathrm{ant}}^{\mathrm{RX},i} \sum_{b\neq g}^{K^{\mathrm{BS}}} \eta_i^{\mathrm{DL}} P_b^{\mathrm{BS}} |h_{i,b}^{\mathrm{DL}}|^2 \\ &\quad + M_{\mathrm{ant}}^{\mathrm{RX},i} \sum_{j_i=1}^{K_{j_i}^{\mathrm{ol}}} \eta_{i,j_i}^{\mathrm{ol}} P_{j_i}^{\mathrm{UL}} |h_{i,j_i}^{\mathrm{DU}}|^2 + P_{n,i}^{\mathrm{DL}}\end{aligned} \tag{46}$$

$$\gamma_j^{\mathrm{UL}} = \eta_j^{\mathrm{UL}} \left(N_{\mathrm{ant}}^{\mathrm{RX}} \sum_{b\neq g}^{K^{\mathrm{BS}}} P_b^{\mathrm{BS}} |h_{g,b}^{\mathrm{BS}}|^2 + P_{\mathrm{RSI},g} + P_{\mathrm{n},g}^{\mathrm{BS}}\right) \tag{47}$$

where $h_{i,g}^{\mathrm{DL}}$, $h_{g,j}^{\mathrm{UL}}$, $h_{i,j}^{\mathrm{DU}}$, and $h_{g,b}^{\mathrm{BS}}$ represent the path losses form BS g to DL user i, form UL user j to BS g, from UL user j to DL user i, and between BS b and BS g, respectively. P_i^{DL}, P_j^{UL}, and P_b^{BS} represent the transmit power for DL user i, transmit power by UL user j, and total transmit power at BS b respectively. $P_{\mathrm{RSI},g}$ is the RSI power after SIC at BS g to capture our SIC effects. $P_{n,i}^{\mathrm{DL}}$ and $P_{\mathrm{n},g}^{\mathrm{BS}}$ are AWGN power at DL user i and BS g. $K_{j_i}^{\mathrm{ol}}$ is the number of UL users which have overlapping with DL user i. η_i^{DL}, η_j^{UL}, and $\eta_{i,j_i}^{\mathrm{ol}}$ capture the ratio of the sub-band of DL user i in the whole bandwidth, the ratio of the sub-band of UL user j in the whole bandwidth, and the ratio of the overlapping portion of sub-bands of DL user i and UL user j_i in the sub-band of DL user i. The optimal user allocation policy is achieved if the sum rate of the network is maximised, which can be cast as

$$\min_{\mathcal{X}} \sum_{i=1}^{K_{\mathrm{DL}}} R_i^{\mathrm{DL}} + \sum_{j=1}^{K_{\mathrm{UL}}} R_j^{\mathrm{UL}} \tag{48}$$

$$s.t. \sum_{t=1}^{T_{\mathrm{DL}}} [x^{\mathrm{DL}}]_{t,i} = 1, \quad \forall\, i \in [1, K_{\mathrm{DL}}] \tag{49}$$

$$\sum_{t=1}^{T_{\mathrm{UL}}} [x^{\mathrm{UL}}]_{t,j} = 1, \quad \forall\, j \in [1, K_{\mathrm{UL}}] \tag{50}$$

where the two constraints force each UE to be allocated to only one sub-band. This problem can be solved by a game theoretic approach [16], where the sum utility of all UEs in this network is given as

$$U(\mathcal{X}) = \sum_{i=1}^{K_{\mathrm{DL}}} R_i^{\mathrm{DL}} + \sum_{j=1}^{K_{\mathrm{UL}}} R_j^{\mathrm{UL}} \tag{51}$$

The sum rate is used as the sum utility instead of the SINR to capture the gain of antenna arrays. The user allocation game is a characteristic formation game with non-transferable utility, which can be solved based on a preference relation as

$$x \prec x'|_{t\leftarrow i} \Leftrightarrow U(\mathcal{X}) < U(\mathcal{X}') \tag{52}$$

where $x \prec x'|_{t\leftarrow i}$ means that UE i is preferred to be allocated into sub-band t instead of its current sub-band. The moving operation will be done if the sum utility increases after UE i moves to sub-band t. We consider each sub-band for UL users will only be occupied by a single user to maximise its capacity since UL eMBB devices require high data throughput. Hence, the UL users can be randomly allocated to these sub-bands at first. Then, each DL user compares the preference with being allocated into all other sub-bands and executes the moving operation if the condition in Equation (52) is satisfied. It should be noted that the indicator of sub-band only determines the order of these sub-bands, while its bandwidth varies with associated users. Performing the compare-and-moving operation for all DL users, the optimal user allocation policy $\bar{\mathcal{S}}$ is obtained. The user allocation algorithm is illustrated as Algorithm 1.

Remark: The user allocation policy mainly depends on the channel strengths, which are strongly dependent on user allocations, so it will be affected by the mobility of users, especially when users move extremely fast. For IIoT scenarios, it is reasonable to assume that users are mostly static or move very slowly that their locations do not change rapidly. Otherwise, the path losses $h_{*,*}^{\dagger}$ must be time-variant to include the effects of user mobility, and some statistical knowledge will be required to calculate the mean sum rate of users.

A. COMPLEXITY

The algorithm is based on the compare-and-moving operations of each DL UE. There is one time of computations

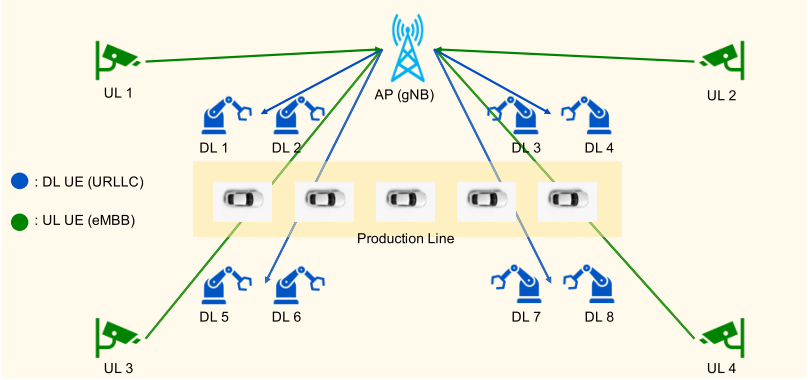

FIGURE 5. A typical IIoT scenario with 4 UL eMBB devices and 8 DL URLLC devices served by a 5G NR AP.

Algorithm 1 User Allocation Algorithm

1: Randomly allocate the UL UEs to associated sub-bands, e.g., $[x^{\mathrm{UL}}]_{t,j} = 1,\ \forall\ t = j \in [1, K_{\mathrm{UL}}]$ and $[x^{\mathrm{UL}}]_{t,j} = 0,\ \forall\ t \neq j \in [1, K_{\mathrm{UL}}]$.
2: Allocate all DL UEs to into a single sub-band, e.g., $[x^{\mathrm{DL}}]_{t,i} = 1,\ \forall\ t = 1,\ i \in [1, K_{\mathrm{DL}}]$ and $[x^{\mathrm{DL}}]_{t,i} = 0,\ \forall\ t \neq 1,\ i \in [1, K_{\mathrm{DL}}]$.
3: Record current user allocation policy $\mathcal{X}$
4: **for all** DL UE $i \in [1, K_{\mathrm{DL}}]$ **do**
5: DL UE i moves into all other sub-band except its current sub-band.
6: Record the new allocation policy after the UE moves as $\mathcal{X}'$.
7: Calculate the sum utilities under the two policy $U(\mathcal{X})$ and $U(\mathcal{X}')$.
8: Compare the preference of the i^{th} DL UE based on the preference relation in Equation (52).
9: **if** the preference relation is satisfied **then**
10: Update the current policy as $\mathcal{X} \leftarrow \mathcal{X}'$.
11: **else**
12: Go back to current policy $\mathcal{X}$.
13: **end if**
14: **end for**

when each DL UE compares the sum utility and determines whether the user is moving. In order to obtain the optimal policy, each of all K_{DL} DL users should move to all other $T_{\mathrm{DL}} - 1$ sub-bands and executes the compare-and-moving operation, which results in a total of $K_{\mathrm{DL}}(T_{\mathrm{DL}} - 1)$ computation times in one cycle. Given a number of cycle times C, the computational complexity of the proposed algorithm is $\mathcal{O}_{\mathrm{UA}}(CK_{\mathrm{DL}}(T_{\mathrm{DL}} - 1))$.

B. CONVERGENCE

Let $\mathcal{X}_0$ denote the initial user allocation policy, and $\mathcal{X}_f$ is the final policy. During the game, the policy is changed as follows:

$$\mathcal{X}_0 \rightarrow \mathcal{X}_1 \rightarrow \mathcal{X}_2 \rightarrow \cdots \rightarrow \mathcal{X}_f \tag{53}$$

TABLE 1. Simulation Parameters.

Parameter	Value
Carrier frequency	28 GHz
Bandwidth	400 MHz
Subcarrier spacing	60 kHz
Number of data subcarriers	1920
FFT size N_{fft}	2048
Number of PDSCH- DMRS	860
Number of OFDM symbols for eMBB devices	14
Number of OFDM symbols for URLCC devices	7 (mini-slot)

Algorithm 1 indicates that the user allocation policy $\mathcal{X}$ will only be changed if the sum utility increases, which suggests that the sum utility is strictly increased with the policy changes in sequence (53) such that

$$U(\mathcal{X}_0) < U(\mathcal{X}_1) < U(\mathcal{X}_2) < \cdots < U(\mathcal{X}_f) \tag{54}$$

As the number of user allocation policies is finite due to the finite number of sub-bands and UEs, the policy in sequence (53) is guaranteed to converge to the local optimal policy.

V. SIMULATION RESULTS

Consider a typical industrial scenario with 4 eMBB devices as UL users, 8 URLLC devices as DL users, and an IBFD enabled 5G NR access point (AP) as shown in Fig. 5. The simulation parameters are taken from 5G NR [30] as shown in Table. 1.

A. LATENCY REDUCTION FOR eMBB DEVICES

In this section, we will do a simple calculation of transmission time (this does not include propagation time, processing time at 5G NR access point, etc.) of eMBB payload shows the advantage of IBFD in terms of reducing latency. For HD systems, the data transmission and reception in FR2 band are based on TDD. It means some part of the slot is used for UL users and the rest is used for DL users. The partition of resources is based on the amount of payload and priority of

TABLE 2. Comparison of Latency of eMBB service with HD and IBFD.

Parameters	# of slots	Transmission Time (ms)
HD (12)	364	91
HD (10)	445	112
HD (7)	667	167
IBFD	308	77

TABLE 3. RF Cancellation Performance.

Bandwidth (MHz)	Number of taps M	η_{RF} (in dB)
50	12	18.56
100	20	17.24
200	32	16.75
400	64	19.59

services. In a typical industry scenario, where sensors and robotics arms are very critical in terms of reliability and latency which act as DL users (URLLC devices), on the other hand, the UL users are CCTV cameras which have a huge amount of data to be transmitted to access point (eMBB devices). Since the payload of URLLC devices is very critical, some part in each slot is reserved even if there is no payload for any slot. These reserved resources tend to increase the latency of eMBB devices. The IBFD enabled 5G NR access point reduces the latency of eMBB devices by simultaneously transmitting and receiving data to URLLC and from eMBB, respectively. In 5G NR, a slot is consists of 14 OFDM symbols of duration 0.25ms for 60 kHz subcarrier spacing and a mini-slot concept for URLLC transmission, which consists of 2, 4, and 7 OFDM symbols. Let us assume that eMBB has 7.68×10^6 samples which are to be transmitted to 5G NR access points with 60 kHz subcarrier spacing, 1920 data subcarriers for 100 MHz bandwidth. Table 2 shows the comparison of IBFD and HD in terms of the number of slots and transmission time of 7.68×10^6 samples with 1920 data subcarriers which require 4000 OFDM symbols. In Table 2, HD (12) represents 12 OFDM symbol (out of which 1 OFDM symbol is used for PDSCH-DMRS) is used by eMBB, and 2 OFDM symbol is used by URLLC. Similarly, HD (10) and HD (7) represents 10 and 7 OFDM symbols are used by eMBB, respectively. In contrast, IBFD used the whole slot (14 OFDM symbols) for the eMBB payload. As observed from Table 2, IBFD reduces the latency (by 54%) by using fewer slots to deliver the same amount of symbols due to the significantly-improved spectral efficiency and always-available time slots.

B. SELF-INTERFERENCE CANCELLATION

Consider a 12-bits ADC at each RF chain, which provides about 67 dB of dynamic range, assuming 10 dB of PAPR of the input signal. The thermal noise density is -174 dBm/Hz, and the noise figure of the access point is 13 dB, which yields a total of -75 dBm noise power with 400 MHz bandwidth. This suggests that the received SI power at the access point has to be suppressed to be at or below -8 dBm to prevent ADC saturation. Assume an access point transmit power of 24 dBm and 15 dB of antenna isolation, then 17 dB of RF cancellation is required to be provided by each canceller in theory. Table 3 shows the required number of constructed delay lines, i.e., taps, to achieve near 20 dB of RF cancellation amount for various bandwidths in FR2 band. The hardware impairments are included in the simulation, where the parameters are taken from some off-the-shelf products available at the ''Thorlabs''. The VOAs have a tuneable range of 30 dB and a tuning step of 0.1 dB.

It is not comprehensive to analyse the effects of RF beamformers on SIC and the relationship between RF and digital cancellation via the channel coefficients estimation error or solely digital cancellation depth, so we demonstrate the total cancellation (antenna isolation, RF and digital cancellation) depth and overall noise floor after SIC in Fig. 6. It illustrates that more subarrays at the receiver may degrade the total cancellation depth, but such degradation is only obvious when the RF cancellation depth is too large (i.e., 90 dB). In contrast, the number of RF chains at the transmitter is more influential on the total cancellation depth, especially when the transceiver distortion is significant. More RF chains at the transmitter can improve the total cancellation performance. We can also see that total cancellation depth does not benefit from further RF cancellation as long as the transceiver distortion is not too large ($\leq$ 50 dB). Although we have concluded that too deep RF cancellation will degrade the digital cancellation performance, it does not degrade the total cancellation performance. From the perspective of overall residual noise, more subarrays at receiver and more RF chains at the transmitter will be preferred as they can reduce the overall noise floor at access points, so provide a better quality of eMBB services. It also illustrates the importance of sufficient RF cancellation. With 0 dB of RF cancellation, even a total of 80 dB of SIC (contributed by about 65 dB of digital cancellation and 15 dB of antenna isolation) can be achieved, and there will be about -40 dBm of residual noise left due to the significant quantisation noise. It should also be noted that at least 30 dB of RF cancellation is required to achieve desired overall SIC (i.e., the total noise floor after SIC is close to the receiver noise floor), while our previous theoretical analysis shows 20 dB of RF cancellation is sufficient. This difference comes from the fact the digital cancellation is not perfect and suffers from channel estimation inaccuracy, which will also be affected by the quantisation noise. Therefore, an 80-taps canceller is utilised to achieve about 30 dB of RF cancellation for later simulations.

C. USER ALLOCATION

We assume all UEs and the AP are equipped with an identical number of transmitting and receiving antennas, and the number of antennas at 5G NR access point, eMBB devices and URLCC devices are 256, 16 and 8, respectively. The access point transmits signals with a total power of 24 dBm averagely allocated to the 8 DL users, and the transmit power at the UL users is 23 dBm. The whole bandwidth

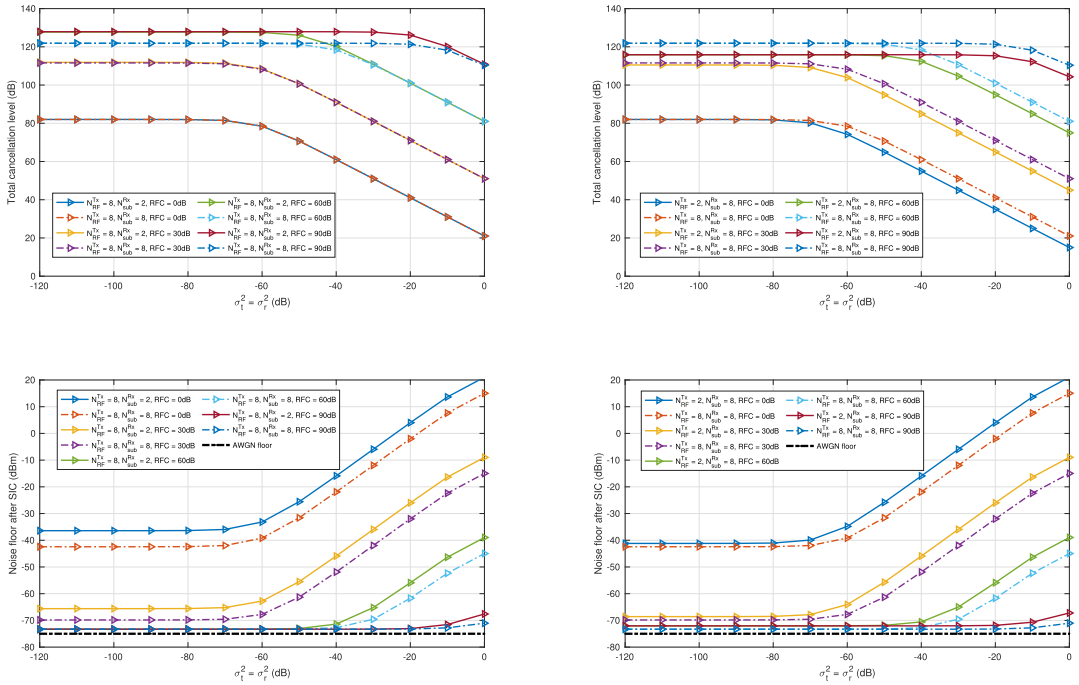

FIGURE 6. Performance evaluation for overall (3-steps) self-interference cancellation.

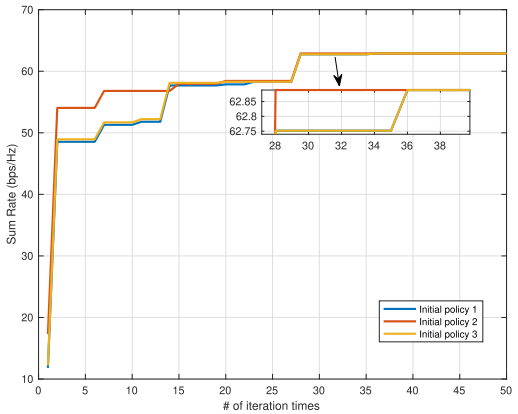

FIGURE 7. Sum rate variation within the user allocation algorithm.

is equally divided into 4 orthogonal sub-bands for both DL and UL users. The path loss model is taken from [31]. After performing the proposed user allocation algorithm, the UEs are allocated to sub-bands as Table 4 shows. It actually allocated the UL users and DL users farthest away from this UL user to the identical sub-band in this simple case. Fig. 7 shows the sum rate variation of this network during the user allocation algorithm with three different random initial user allocation policies, which proves the convergence behaviour. Different initial policies may result in different policy changing sequences but will converge to the same final optimal policy.

D. BER AND SE EVALUATION

In this section, we evaluate the system-level performance of this network in terms of average BER and SE through

TABLE 4. Optimal User Allocation Policy.

Sub-bands	UL UEs	DL UEs
sub-band 1 (27.8-27.9 GHz)	4	1, 2
sub-band 2 (27.9-28.0 GHz)	3	3, 4
sub-band 3 (28.0-28.1 GHz)	2	5, 6
sub-band 4 (28.1-28.2 GHz)	1	7, 8

practical simulations. It should be noted that the performance will be similar in the 4 sub-bands since they have identical configurations, so the performance for URLCC devices can be evaluated by the pair on a single sub-band, e.g., pair 1 (DL users 1 and 2) on sub-band 1. Antennas at 5G NR access points are divided into 4 subarrays, and each subarray has an equal number (64) of non-overlap antenna elements connected to one RF chain, and both eMBB and URLLC devices have only one subarray connected to one RF chain. We have considered 4 eMBB devices, with each having non-overlapping 100 MHz bandwidth and either QPSK or 16-QAM modulated payload. On the other hand, we have considered 4 pairs (total 8) URLCC devices, with each having non-overlapping 100 MHz bandwidth. Each pair of URLLC receives a payload at the same time and frequency. To guarantee the orthogonality of the 2 URLLC devices in each pair, the payload of one device is BPSK $(-1,+1)$ modulated, while the other is $\pi/2-$BPSK $(-1\mathrm{i},+1\mathrm{i})$ modulated. In this way, the four subarrays of 5G NR access points simultaneously transmit data to the four pairs of URLCC devices and receive data from the four eMBB devices with the SIC applied. The transmit and receive antennas at the 5G NR access point are orthogonally

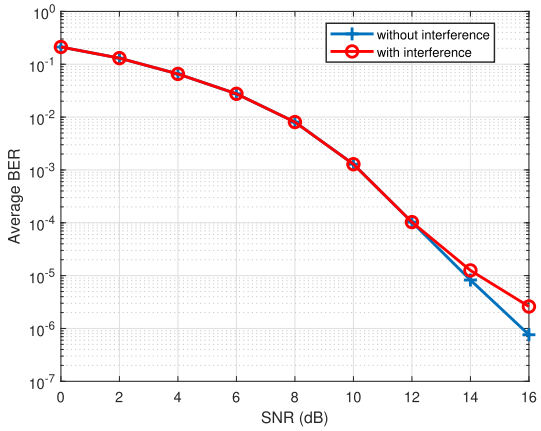

(a) Average BER vs SNR of pair 1 of URLLC.

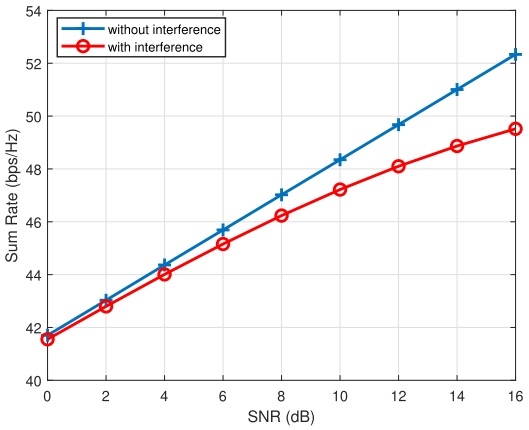

(b) SE vs SNR of pair 1 of URLLC.

FIGURE 8. Performance evaluation of URLLC services.

polarised. PDSCH data is low density parity check (LDPC) encoded with code rate 1/3. The height of 5G NR access point, eMBB device, and URLCC device are 15m, 7m, and 2m, respectively.

Fig. 8(a) shows the average BER vs SNR of pair 1 of URLCC devices with and without interference. The interference to the pair of URLCC devices is the CCI from corresponding eMBB devices. Only RF precoding and combining are used, and their weights are pre-calculated according to their known coordinates. It is observed from the figure that there is an error floor in BER in the presence of interference, i.e., there is no significant difference for scenarios with and without CCI when SNR$<$ 12 dB. The reason is that the CCI has been mitigated by the user allocation policy and highly directional beams due to RF beamforming, so the CCI is below the receiver noise floor when SNR is low (i.e., transmit power is small). It shows that $\geq$ 99.99999% reliability can be achieved with SNR $\geq$ 16 dB with the minimised CCI in our network, while about 20 dB of SNR can be achieved as long as the URLLC devices are within 50 m of the access point. Fig. 8(b) shows the SE vs SNR of pair 1 of URLCC devices with and without interference. The achievable SE of the HD radios is half of the blue curve (without interference), while the red curve (with interference) is the achievable SE of the IBFD radios with the optimal user allocation policy and RF beamformers (i.e., mitigated CCI). With SNR $>$ 10 dB ($>$ 45 bps/Hz SE), 56 kHz bandwidth is sufficient to deliver 2.5 Mbps of throughput, while 103 kHz is needed for HD radios. This indicates that the IBFD can almost double the connection density for specific throughput. The interference can be further mitigated by transmitting a pencil beam to the desired user using more number of antennas, digital beamforming as in [7] and [11], or advanced signal processing such as interference alignment in [15], thus, further improve the quality of URLLC service.

Fig. 9 shows the average BER vs SNR of pair 1 of eMBB devices with various quantisation and modulation conditions in the presence of all noise and distortions (i.e., AWGN, transceiver distortion, canceller distortions and RSI), where the x-axis of Fig. 9(a) and Fig. 9(c) means the RSI after RF cancellation is x dB higher than the received SoI. Fig. 9(b) and Fig. 9(d) are derived with 14 dB and 20 dB of SNR respectively, and Fig. 9(b) and Fig. 9(d) are derived with received SI 35 dB higher than the received SoI. Fig. 9(a) and Fig. 9(b) show results for QPSK modulation, while Fig. 9(c) and Fig. 9(d) show results for 16QAM modulation.It can be seen that high quantisation resolution (more effective bits of ADCs) is essential to deliver highly reliable services if the RF cancellation is not deep enough (e.g., the RSI is 30 dB higher than the received signal of interest due to insufficient RF cancellation). Typically, 20 dB of RF cancellation will be required to eliminate the effects of dynamic range of ADCs (12 bits) for QPSK, and this value increases to 30 dB for 16-QAM. Also, this value increases with decreasing number of effect bits of ADCs. $\geq$ 99.9999% reliability can be achieved with SNR $\geq$ 13 dB for QPSK, and SNR $\geq$ 20 dB for 16-QAM. Fig. 10 shows the SE vs SNR of eMBB devices in the presence of all noise and distortions with 12-bits ADCs and RSI 35 dB higher than the received SoI. It demonstrates that 2.5 Gbps data rate can be achieved with 400 MHz communication bandwidth even with SNR $=$ 0 dB for eMBB devices due to the enormous resources provided by the FR2 band, IBFD radios, and large antenna arrays. Furthermore, the effects of the limited dynamic range of ADCs on the SE is not as significant as on the BER that it is almost invisible at low SNR. This suggests that too deep RF cancellation is not extremely critical for eMBB service, which does not have stringent requirements for reliability. Besides, Fig. 8(b) and Fig. 10 in conjunction with the reduction of 4 dB SNR of UL signals indicate that IBFD radios achieve about 1.92 times SE of HD radios with our SIC scheme and user allocation policy.

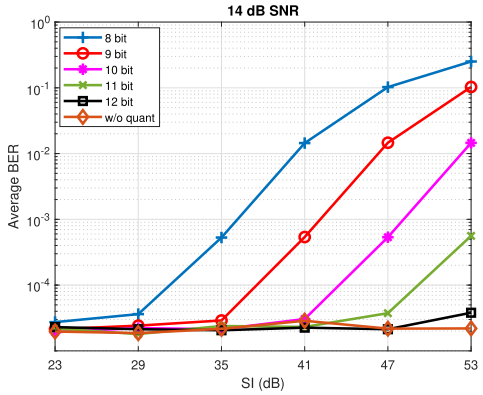

(a) Average BER vs RSI (QPSK).

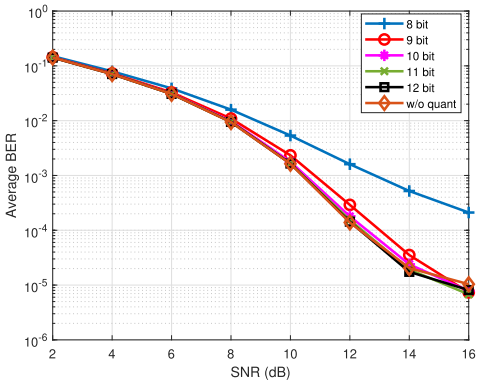

(b) Average BER vs SNR (QPSK).

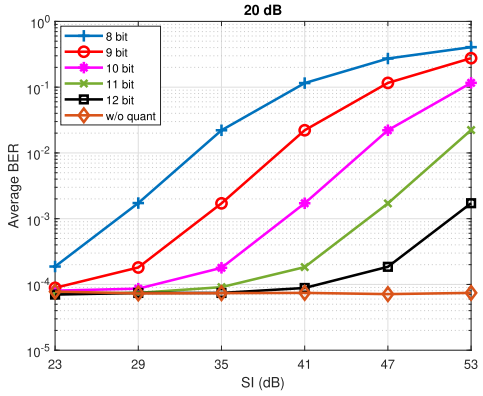

(c) Average BER vs RSI (16QAM).

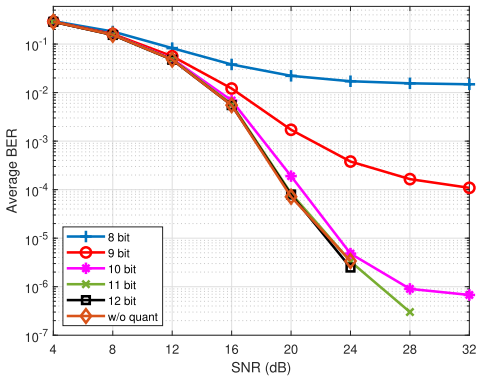

(d) Average BER vs SNR (16QAM).

FIGURE 9. Performance evaluation of eMBB with ADC effects.

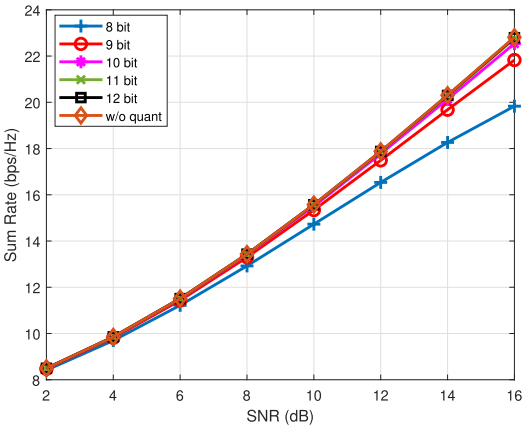

FIGURE 10. SE vs SNR of eMBB devices with ADC effects.

VI. CONCLUSION

In this paper, we proposed signal processing techniques to reduce the SI and CCI for full-duplex private 5G networks in FR2 band and evaluated its performance in terms of throughput, latency, reliability, and device density under a typical industrial scenario. Large-scale antenna arrays are essential to compensate for the large path loss in FR2 band, and RF beamforming is applied to save the cost. RF cancellation also benefited from the RF beamforming to reduce the number of cancellers, but each canceller will need more taps to mimic the effective SI channel, whose RMS delay spread is enlarged due to RF beamforming. For digital cancellation, its performance is affected by the number of transmitter RF chains, the number of subarrays at receiver, transceiver distortions, and RF cancellation. More RF chains at the transmitter, more subarrays at the receiver, and deeper RF cancellation are always wanted to reduce the overall noise induced by the SI. However, it hardly has more benefits from more than 30 dB of RF cancellation when transceiver distortion is not too large. On the other hand, the CCI is efficiently mitigated through the user allocation policy and highly directional beams formed by RF beamformers, providing highly reliable URLLC services. Such efficient IBFD radios provide the private 5G network with 1.92 times throughput and almost doubled device density compared to HD radios and reduce latency of UL eMBB devices by half. Utilising 4× scaled numerology (60 kHz of subcarrier spacing), mini-slot (7 symbols in a slot), and self-contained sub-frames in 5G NR standard, we theoretically analyse that the latency of DL URLLC devices can be reduced to be within 0.5 ms and simulation results demonstrate its reliability to be $\geq$ 99.99999%. Numerical results also show that multi-Gbps peak data rates can be achieved by eMBB devices. However, these results are derived with

theoretical models and hypothetical values of some parameters while lacking the practical hardware impairments effects. The future direction of this work should be implementing the SIC scheme in practice and evaluating the performance with practical hardware impairments, and adapting 3GPP channel models under specific scenarios (e.g., urban-micro (UMi) or indoor hotspot (InH)). To sum up, our proposed SIC and user allocation techniques can enable IBFD private 5G NR standard Networks in FR2 band for heterogeneous IIoT environment, which supports massive connectivity, enhanced ultra-reliable low latency communications, and multi-Gbps data rates for eMBB and its practical performance is supposed to be evaluated in future.

APPENDIX A
NECESSARY NOTATIONS

Table 5 gives a tabular form for necessary notations.

TABLE 5. Essential notations and corresponding descriptions.

Symbol	Description
a_i	complex coefficient induced by the RF beamformer at the i^{th} antenna
$\alpha_{ij,l}$	attenuation of the l^{th} path between the i^{th} receive antenna and the j^{th} transmit antenna
b	number of effective bits of ADCs
d_{rs}	distance between the s^{th} transmit antenna and r^{th} receive antenna
$D^{\text{RF}}_{ij,g,k}$	RF SIC depth at the k^{th} subcarrier of the SI channel between the j^{th} transmit antenna to the i^{th} receive antenna at the g^{th} BS
$D^{\text{dig}}_{g,k}$	digital SIC depth at the k^{th} subcarrier of the SI channel at the g^{th} BS
K	Rician factor
K_c	number of subcarriers
K_{BS}	number of base stations
K_{DL} / K_{UL}	number of downlink / uplink UEs served by a BS
l^{SI}_g	pathloss of the SI channel at the g^{th} BS
L	number of clusters
M	number of taps
M_n	number of rays in the n^{th} cluster
$M^{\text{Tx}}_{\text{ant},j}$ / $M^{\text{Rx}}_{\text{ant},j}$	number of transmit / receive antennas at the j^{th} uplink / downlink UE
$M^{\text{Tx}}_{\text{RF},j}$ / $M^{\text{Rx}}_{\text{RF},j}$	number of RF chains at the transmitter / receiver of the j^{th} uplink / downlink UE
$M^{\text{Tx}}_{\text{sub},j}$ / $M^{\text{Rx}}_{\text{sub},j}$	number of subarrays at the transmit / receive antenna array of the j^{th} uplink / downlink UE
$N^{\text{Tx}}_{\text{sym}}$	number of data symbols transmitted to DL users
$N^{\text{Rx}}_{\text{sym}}$	number of data symbols received from UL users
$N^{\text{Tx}}_{\text{ant}}$ / $N^{\text{Rx}}_{\text{ant}}$	number of transmit / receive antennas at the BS
$N^{\text{Tx}}_{\text{RF}}$ / $N^{\text{Rx}}_{\text{RF}}$	number of RF chains at the transmitter / receiver of the BS
$N^{\text{Tx}}_{\text{sub}}$ / $N^{\text{Rx}}_{\text{sub}}$	number of subarrays at the transmit / receive antenna array of the BS
$N^{\text{Tx}}_{\text{cnt},l}$ / $N^{\text{Rx}}_{\text{cnt},l}$	number of RF chains connected to the l^{th} subarray at the transmit / receive antenna array of the BS
P_{BS} / P_{UE}	transmit power of the BS / UE
$t_{ij,l}$	delay of the l^{th} path between the i^{th} receive antenna and the j^{th} transmit antenna
τ_n / τ_{m_n}	delay of the n^{th} cluster / m^{th}_n ray
ρ	quantisation noise factor
η^{RF}_g	average RF cancellation depth at the g^{th} BS
σ^2_t / σ^2_r	transmitter / receiver distortion factor
σ^2_{BS} / σ^2_{UE}	AWGN floor at the BS / UE
σ^2_{canc}	noise and distortions floor introduced by RF cancellers

APPENDIX B
RF BEAMFORMER PROPERTIES

The RF beamformers are implemented via phase shifters in practice, which only adjusts the phase of the input signal, so each non-zero element of the RF beamformers can be described as $e^{j\theta}$, where $\theta \sim U(0, 2\pi)$. Assume f_m and f_n are two non-zero elements of the RF precoder matrix $\mathbf{F}_{\text{RF}}$, then we have $\mathbb{E}\{f_m f_n^*\} = f_m f_n^* = 1$ if $m = n$. For the case that $m \neq n$, we have $\mathbb{E}\{f_m f_n^*\} = \mathbb{E}\{e^{j\theta_m} e^{-j\theta_n}\} = \mathbb{E}\{e^{j(\theta_m-\theta_n)}\}$, where the probability density function of $x = \theta_m - \theta_n$ is given as

$$f(x) = \begin{cases} \frac{1}{4\pi^2}x + \frac{1}{2\pi}, & \text{if } -2\pi \le x < 0 \\ -\frac{1}{4\pi^2}x + \frac{1}{2\pi}, & \text{if } 0 \le x \le 2\pi \end{cases} \tag{55}$$

so that we have

$$\begin{aligned} \mathbb{E}\left\{e^{j(\theta_m-\theta_n)}\right\} &= \int_{-2\pi}^{2\pi} e^{jx} f(x) dx \\ &= \int_{-2\pi}^{0} e^{jx}\left(\frac{1}{4\pi^2}x + \frac{1}{2\pi}\right) dx \\ &\quad + \int_{0}^{2\pi} e^{jx}\left(-\frac{1}{4\pi^2}x + \frac{1}{2\pi}\right) dx \\ &= \left[\frac{1}{2\pi j}e^{jx} + \frac{jx}{4\pi^2}e^{jx} - \frac{1}{4\pi^2}e^{jx}\right]_{-2\pi}^{0} \\ &\quad + \left[\frac{1}{2\pi j}e^{jx} - \frac{jx}{4\pi^2}e^{jx} + \frac{1}{4\pi^2}e^{jx}\right]_{0}^{2\pi} = 0 \end{aligned}$$

Therefore, we can derive that

$$\begin{aligned} &\mathbb{E}\left\{\mathbf{F}^{\text{BS},g}_{\text{RF}}\left(\mathbf{F}^{\text{BS},g}_{\text{RF}}\right)^H\right\} \\ &= \mathcal{D}\left(N^{\text{Tx}}_{\text{cnt},1}\mathbf{I}_{N^{\text{Tx}}_{\text{ant,sub}}}, N^{\text{Tx}}_{\text{cnt},2}\mathbf{I}_{N^{\text{Tx}}_{\text{ant,sub}}}, \ldots, N^{\text{Tx}}_{\text{cnt},N^{\text{Tx}}_{\text{sub}}}\mathbf{I}_{N^{\text{Tx}}_{\text{ant,sub}}}\right) \end{aligned} \tag{56}$$

$$tr\left(\mathbb{E}\left\{\mathbf{F}^{\text{BS},g}_{\text{RF}}\left(\mathbf{F}^{\text{BS},g}_{\text{RF}}\right)^H\right\}\right) = \frac{N^{\text{Tx}}_{\text{ant}}N^{\text{Tx}}_{\text{RF}}}{N^{\text{Tx}}_{\text{sub}}} \tag{57}$$

Similarly, we can derive

$$\mathbb{E}\left\{\left(\mathbf{W}^{\text{BS},g}_{\text{RF}}\right)^H \mathbf{W}^{\text{BS},g}_{\text{RF}}\right\} = \frac{N^{\text{Rx}}_{\text{ant}}}{N^{\text{Rx}}_{\text{sub}}}\mathbf{I}_{N^{\text{Rx}}_{\text{RF}}} \tag{58}$$

$$tr\left(\mathbb{E}\left\{\left(\mathbf{W}^{\text{BS},g}_{\text{RF}}\right)^H \mathbf{W}^{\text{BS},g}_{\text{RF}}\right\}\right) = \frac{N^{\text{Rx}}_{\text{ant}}N^{\text{Rx}}_{\text{RF}}}{N^{\text{Rx}}_{\text{sub}}} \tag{59}$$

APPENDIX C
STATISTICS OF ESTIMATION ERROR

In this appendix, we will derive the statistics of the channel estimation error during the digital cancellation, and we will ignore the frequency index here since the statistics are identical for each subcarrier.

$$\begin{aligned} &\mathbb{E}\{\Delta_{\text{eff},g}\} \\ &= \mathbb{E}\left\{\mathbf{H}^{\text{eff}}_{\text{RSI},g} - \widehat{\mathbf{H}}^{\text{eff}}_{\text{RSI},g}\right\} \\ &= \mathbb{E}\left\{\mathbf{H}^{\text{eff}}_{\text{RSI},g} - \left(\mathbf{H}^{\text{eff}}_{\text{RSI},g}s^{\text{BS}}_g + \tilde{\mathbf{n}}^{\text{BS}}_g\right)\left((s^{\text{BS}}_g)^H s^{\text{BS}}_g\right)^{-1}(s^{\text{BS}}_g)^H\right\} \end{aligned}$$

$$= \mathbb{E}\left\{\mathbf{H}_{\mathrm{RSI},g}^{\mathrm{eff}}\right\} - \mathbb{E}\left\{\mathbf{H}_{\mathrm{RSI},g}^{\mathrm{eff}} s_g^{\mathrm{BS}} \left((s_g^{\mathrm{BS}})^H s_g^{\mathrm{BS}}\right)^{-1} (s_g^{\mathrm{BS}})^H\right\}$$
$$-\mathbb{E}\left\{\widetilde{\mathbf{n}}_g^{\mathrm{BS}} \left((s_g^{\mathrm{BS}})^H \mathbf{s}_g^{\mathrm{BS}}\right)^{-1} (s_g^{\mathrm{BS}})^H\right\} = \mathbf{0}$$

$$var\left\{\Delta_{\mathrm{eff},g}\right\}$$
$$= \mathbb{E}\left\{\left(\Delta_{\mathrm{eff},g} - \mathbb{E}\left\{\Delta_{\mathrm{eff},g}\right\}\right)\left(\Delta_{\mathrm{eff},g} - \mathbb{E}\left\{\Delta_{\mathrm{eff},g}\right\}\right)^H\right\}$$
$$= \mathbb{E}\left\{\left(\mathbf{H}_{\mathrm{RSI},g}^{\mathrm{eff}} - \widehat{\mathbf{H}}_{\mathrm{RSI},g}^{\mathrm{eff}}\right)\left(\mathbf{H}_{\mathrm{RSI},g}^{\mathrm{eff}} - \widehat{\mathbf{H}}_{\mathrm{RSI},g}^{\mathrm{eff}}\right)^H\right\}$$
$$= \mathbb{E}\left\{\mathbf{H}_{\mathrm{RSI},g}^{\mathrm{eff}}\left(\mathbf{H}_{\mathrm{RSI},g}^{\mathrm{eff}}\right)^H\right\} - \mathbb{E}\left\{\mathbf{H}_{\mathrm{RSI},g}^{\mathrm{eff}}\left(\widehat{\mathbf{H}}_{\mathrm{RSI},g}^{\mathrm{eff}}\right)^H\right\}$$
$$-\mathbb{E}\left\{\widehat{\mathbf{H}}_{\mathrm{RSI},g}^{\mathrm{eff}}\left(\mathbf{H}_{\mathrm{RSI},g}^{\mathrm{eff}}\right)^H\right\} + \mathbb{E}\left\{\widehat{\mathbf{H}}_{\mathrm{RSI},g}^{\mathrm{eff}}\left(\widehat{\mathbf{H}}_{\mathrm{RSI},g}^{\mathrm{eff}}\right)^H\right\}$$

So, the estimation error is a zero-mean complex Gaussian variable, whose variance is given in detail as (assume the intended transmit signal is independent from all transceiver distortions and noise)

$$\mathbb{E}\left\{\mathbf{H}_{\mathrm{RSI},g}^{\mathrm{eff}}\left(\widehat{\mathbf{H}}_{\mathrm{RSI},g}^{\mathrm{eff}}\right)^H\right\}$$
$$= \mathbb{E}\left\{\mathbf{H}_{\mathrm{RSI},g}^{\mathrm{eff}}\left(\left(\mathbf{H}_{\mathrm{RSI},g}^{\mathrm{eff}} s_g^{\mathrm{BS}} + \mathbf{n}_g^{\mathrm{BS}}\right)\left((s_g^{\mathrm{BS}})^H s_g^{\mathrm{BS}}\right)^{-1}(s_g^{\mathrm{BS}})^H\right)^H\right\}$$
$$= \mathbb{E}\left\{\mathbf{H}_{\mathrm{RSI},g}^{\mathrm{eff}} s_g^{\mathrm{BS}}\left((s_g^{\mathrm{BS}})^H s_g^{\mathrm{BS}}\right)^{-1}(s_g^{\mathrm{BS}})^H\left(\mathbf{H}_{\mathrm{RSI},g}^{\mathrm{eff}}\right)^H\right\}$$
$$+\mathbb{E}\left\{\mathbf{H}_{\mathrm{RSI},g}^{\mathrm{eff}} s_g^{\mathrm{BS}}\left((s_g^{\mathrm{BS}})^H s_g^{\mathrm{BS}}\right)^{-1}(\widetilde{\mathbf{n}}_g^{\mathrm{BS}})^H\right\}$$
$$= \mathbb{E}\left\{\mathbf{H}_{\mathrm{RSI},g}^{\mathrm{eff}}\left(\mathbf{H}_{\mathrm{RSI},g}^{\mathrm{eff}}\right)^H\right\}$$

Similarly, $\mathbb{E}\left\{\widehat{\mathbf{H}}_{\mathrm{RSI},g}^{\mathrm{eff}}\left(\mathbf{H}_{\mathrm{RSI},g}^{\mathrm{eff}}\right)^H\right\} = \mathbb{E}\left\{\mathbf{H}_{\mathrm{RSI},g}^{\mathrm{eff}}\left(\mathbf{H}_{\mathrm{RSI},g}^{\mathrm{eff}}\right)^H\right\}$.

$$\mathbb{E}\left\{\widehat{\mathbf{H}}_{\mathrm{RSI},g}^{\mathrm{eff}}\left(\widehat{\mathbf{H}}_{\mathrm{RSI},g}^{\mathrm{eff}}\right)^H\right\}$$
$$= \mathbb{E}\left\{y_{\mathrm{RSI}}^{\mathrm{BS},g}\left((s_g^{\mathrm{BS}})^H s_g^{\mathrm{BS}}\right)^{-1}\left(y_{\mathrm{RSI}}^{\mathrm{BS},g}\right)^H\right\}$$
$$= \mathbb{E}\left\{\left(\mathbf{H}_{\mathrm{RSI},g}^{\mathrm{eff}} s_g^{\mathrm{BS}} + \widetilde{\mathbf{n}}_g^{\mathrm{BS}}\right)\left((s_g^{\mathrm{BS}})^H s_g^{\mathrm{BS}}\right)^{-1}\right.$$
$$\left.\times\left(\mathbf{H}_{\mathrm{RSI},g}^{\mathrm{eff}} s_g^{\mathrm{BS}} + \widetilde{\mathbf{n}}_g^{\mathrm{BS}}\right)^H\right\}$$
$$= \mathbb{E}\left\{\mathbf{H}_{\mathrm{RSI},g}^{\mathrm{eff}}\left(\mathbf{H}_{\mathrm{RSI},g}^{\mathrm{eff}}\right)^H\right\}$$
$$+\mathbb{E}\left\{\widetilde{\mathbf{n}}_g^{\mathrm{BS}}\left((s_g^{\mathrm{BS}})^H s_g^{\mathrm{BS}}\right)^{-1}\left(\widetilde{\mathbf{n}}_g^{\mathrm{BS}}\right)^H\right\}$$
$$= \mathbb{E}\left\{\mathbf{H}_{\mathrm{RSI},g}^{\mathrm{eff}}\left(\mathbf{H}_{\mathrm{RSI},g}^{\mathrm{eff}}\right)^H\right\} + \frac{1}{P_{\mathrm{BS}}}\mathbb{E}\left\{\widetilde{\mathbf{n}}_g^{\mathrm{BS}}\left(\widetilde{\mathbf{n}}_g^{\mathrm{BS}}\right)^H\right\}$$

It is reasonable to assume that the residual received signal $\widetilde{\mathbf{y}}_{\mathrm{RSI}}^{\mathrm{BS},g}$ is dominated by the RSI (i.e., $\widetilde{\mathbf{y}}_{\mathrm{RSI}}^{\mathrm{BS},g} \approx H_{\mathrm{RSI},g}^{\mathrm{eff}} s_g^{\mathrm{BS}}$), and the transceiver distortions, noise, and nonlinearities of cancellers are independent from each other, so that

$$\mathbb{E}\left\{\widetilde{\mathbf{n}}_g^{\mathrm{BS}}\left(\widetilde{\mathbf{n}}_g^{\mathrm{BS}}\right)^H\right\}$$
$$= \mathbb{E}\left\{\mathbf{H}_{\mathrm{RSI},g}^{\mathrm{eff}}\mathbf{t}_g^{\mathrm{BS}}\left(\mathbf{t}_g^{\mathrm{BS}}\right)^H\left(\mathbf{H}_{\mathrm{RSI},g}^{\mathrm{eff}}\right)^H\right\}$$
$$+\mathbb{E}\left\{\mathbf{n}_g^{\mathrm{BS}}\left(\mathbf{n}_g^{\mathrm{BS}}\right)^H\right\} + \mathbb{E}\left\{\mathbf{n}_g^{\mathrm{canc}}\left(\mathbf{n}_g^{\mathrm{canc}}\right)^H\right\}$$
$$+\mathbb{E}\left\{\mathbf{n}_g^{\mathrm{qtz}}\left(\mathbf{n}_g^{\mathrm{qtz}}\right)^H\right\} + \mathbb{E}\left\{\mathbf{r}_g^{\mathrm{BS}}\left(\mathbf{r}_g^{\mathrm{BS}}\right)^H\right\}$$
$$= \sigma_t^2\mathbb{E}\left\{\mathbf{H}_{\mathrm{RSI},g}^{\mathrm{eff}}\mathcal{D}\left(\mathbf{F}_{\mathrm{RF}}^{\mathrm{BS},g}\mathbf{s}_g^{\mathrm{BS}}(\mathbf{s}_g^{\mathrm{BS}})^H(\mathbf{F}_{\mathrm{RF}}^{\mathrm{BS},g})^H\right)(\mathbf{H}_{\mathrm{RSI},g}^{\mathrm{eff}})^H\right\}$$
$$+(\sigma_{\mathrm{canc}}^2 + \sigma_{\mathrm{BS}}^2)\mathbf{I}_{N_{\mathrm{RF}}^{\mathrm{Rx}}} + \sigma_r^2\cdot\mathbb{E}\left\{\mathcal{D}\left(\widetilde{\mathbf{y}}_{\mathrm{RSI}}^{\mathrm{BS},g}\left(\widetilde{\mathbf{y}}_{\mathrm{RSI}}^{\mathrm{BS},g}\right)^H\right)\right\}$$
$$+\rho(1-\rho)\cdot\mathbb{E}\left\{\mathcal{D}\left(\widetilde{\mathbf{y}}_{\mathrm{RSI}}^{\mathrm{BS},g}\left(\widetilde{\mathbf{y}}_{\mathrm{RSI}}^{\mathrm{BS},g}\right)^H\right)\right\}$$
$$\approx \sigma_t^2\frac{P_{\mathrm{BS}}}{N_{\mathrm{RF}}^{\mathrm{Tx}}}\mathbb{E}\left\{\mathbf{H}_{\mathrm{RSI},g}^{\mathrm{eff}}\mathbf{F}_{\mathrm{RF}}^{\mathrm{BS},g}(\mathbf{F}_{\mathrm{RF}}^{\mathrm{BS},g})^H(\mathbf{H}_{\mathrm{RSI},g}^{\mathrm{eff}})^H\right\}$$
$$+(\sigma_{\mathrm{canc}}^2 + \sigma_{\mathrm{BS}}^2)\mathbf{I}_{N_{\mathrm{RF}}^{\mathrm{Rx}}}$$
$$+\left(\rho(1-\rho) + \sigma_r^2\right)\frac{P_{\mathrm{BS}}l_g^{\mathrm{SI}}}{(1+\sigma_t^2)\eta_g^{\mathrm{RF}}}\frac{N_{\mathrm{ant}}^{\mathrm{Rx}}}{N_{\mathrm{sub}}^{\mathrm{Rx}}}\mathbf{I}_{N_{\mathrm{RF}}^{\mathrm{Rx}}}$$
$$= \sigma_t^2\frac{P_{\mathrm{BS}}}{N_{\mathrm{RF}}^{\mathrm{Tx}}}\frac{l_g^{\mathrm{SI}}}{(1+\sigma_t^2)\eta_g^{\mathrm{RF}}}\frac{N_{\mathrm{RF}}^{\mathrm{Tx}}N_{\mathrm{ant}}^{\mathrm{Rx}}}{N_{\mathrm{sub}}^{\mathrm{Rx}}}\mathbf{I}_{N_{\mathrm{RF}}^{\mathrm{Rx}}} + (\sigma_{\mathrm{canc}}^2 + \sigma_{\mathrm{BS}}^2)\mathbf{I}_{N_{\mathrm{RF}}^{\mathrm{Rx}}}$$
$$+\left(\rho(1-\rho) + \sigma_r^2\right)\frac{P_{\mathrm{BS}}l_g^{\mathrm{SI}}}{(1+\sigma_t^2)\eta_g^{\mathrm{RF}}}\frac{N_{\mathrm{ant}}^{\mathrm{Rx}}}{N_{\mathrm{sub}}^{\mathrm{Rx}}}\mathbf{I}_{N_{\mathrm{RF}}^{\mathrm{Rx}}}$$
$$= \left(P_{\mathrm{BS}}\frac{(\sigma_t^2 + \sigma_r^2 + \rho(1-\rho))l_g^{\mathrm{SI}}}{(1+\sigma_t^2)\eta_g^{\mathrm{RF}}}\frac{N_{\mathrm{ant}}^{\mathrm{Rx}}}{N_{\mathrm{sub}}^{\mathrm{Rx}}} + \sigma_{\mathrm{canc}}^2 + \sigma_{\mathrm{BS}}^2\right)\mathbf{I}_{N_{\mathrm{RF}}^{\mathrm{Rx}}}$$

where l_g^{SI} denotes the pathloss of the SI channel, such that $\mathbf{H}_{\mathrm{SI},g} \sim \mathcal{CN}\left(\mathbf{0}, l_g^{\mathrm{SI}}\cdot\mathbf{I}_{N_{\mathrm{ant}}^{\mathrm{Rx}}}\right)$. Finally, we have

$$var\left\{\Delta_{\mathrm{eff},g}\right\}$$
$$= \frac{1}{P_{\mathrm{BS}}}\mathbb{E}\left\{\widetilde{\mathbf{n}}_g^{\mathrm{BS}}\left(\widetilde{\mathbf{n}}_g^{\mathrm{BS}}\right)^H\right\}$$
$$= \left(\frac{\left(\sigma_t^2 + \sigma_r^2 + \rho(1-\rho)\right)l_g^{\mathrm{SI}}N_{\mathrm{ant}}^{\mathrm{Rx}}}{(1+\sigma_t^2)\eta_g^{\mathrm{RF}}N_{\mathrm{sub}}^{\mathrm{Rx}}} + \frac{\sigma_{\mathrm{canc}}^2 + \sigma_{\mathrm{BS}}^2}{P_{\mathrm{BS}}}\right)\mathbf{I}_{N_{\mathrm{RF}}^{\mathrm{Rx}}} \tag{60}$$

REFERENCES

[1] A. Aijaz, "Private 5G: The future of industrial wireless," *IEEE Ind. Electron. Mag.*, vol. 14, no. 4, pp. 136–145, Dec. 2020.
[2] E. Markoval, D. Moltchanov, R. Pirmagomedov, D. Ivanova, Y. Koucheryavy, and K. Samouylov, "Priority-based coexistence of eMBB and URLLC traffic in industrial 5G NR deployments," in *Proc. 12th Int. Congr. Ultra Modern Telecommun. Control Syst. Workshops (ICUMT)*, Oct. 2020, pp. 1–6.
[3] H. Ji, S. Park, J. Yeo, Y. Kim, J. Lee, and B. Shim, "Ultra-reliable and low-latency communications in 5G downlink: Physical layer aspects," *IEEE Wireless Commun.*, vol. 25, no. 3, pp. 124–130, Jun. 2018.
[4] A. Bishnu, M. Holm, and T. Ratnarajah, "Performance evaluation of full-duplex IAB multi-cell and multi-user network for FR2 band," *IEEE Access*, vol. 9, pp. 72269–72283, 2021.
[5] J. Zhang, N. Garg, M. Holm, and T. Ratnarajah, "Design of full duplex millimeter-wave integrated access and backhaul networks," *IEEE Wireless Commun.*, vol. 28, no. 1, pp. 60–67, Feb. 2021.

[6] T. Zhang, S. Biswas, and T. Ratnarajah, "An analysis on wireless edge caching in in-band full-duplex FR2-IAB networks," *IEEE Access*, vol. 8, pp. 164987–165002, 2020.
[7] P. Aquilina, A. C. Cirik, and T. Ratnarajah, "Weighted sum rate maximization in full-duplex multi-user multi-cell MIMO networks," *IEEE Trans. Commun.*, vol. 65, no. 4, pp. 1590–1608, Apr. 2017.
[8] H. Luo, M. Holm, and T. Ratnarajah, "Wideband active analog self-interference cancellation for 5G and beyond full-duplex systems," in *Proc. 54th Asilomar Conf. Signals, Syst., Comput.*, Nov. 2020, pp. 868–872.
[9] Z. Ni, J. A. Zhang, K. Yang, F. Gao, and J. An, "Hybrid precoder design with minimum-subspace-distortion quantization in multiuser mmWave communications," *IEEE Trans. Veh. Technol.*, vol. 69, no. 10, pp. 11055–11065, Oct. 2020.
[10] H. Luo, M. Holm, and T. Ratnarajah, "On the performance of active analog self-interference cancellation techniques for beyond 5G systems," *China Commun.*, vol. 18, no. 10, pp. 158–168, Oct. 2021.
[11] J. Zhang, H. Luo, N. Garg, A. Bishnu, M. Holm, and T. Ratnarajah, "Design and analysis of wideband in-band-full-duplex FR2-IAB networks," *IEEE Trans. Wireless Commun.*, to be published.
[12] K. Komatsu, Y. Miyaji, and H. Uehara, "Iterative nonlinear self-interference cancellation for in-band full-duplex wireless communications under mixer imbalance and amplifier nonlinearity," *IEEE Trans. Wireless Commun.*, vol. 19, no. 7, pp. 4424–4438, Jul. 2020.
[13] Y. Kurzo, A. T. Kristensen, A. Burg, and A. Balatsoukas-Stimming, "Hardware implementation of neural self-interference cancellation," *IEEE J. Emerg. Sel. Topics Circuits Syst.*, vol. 10, no. 2, pp. 204–216, Jun. 2020.
[14] Y. Jiang, H. Duan, X. Zhu, Z. Wei, T. Wang, F.-C. Zheng, and S. Sun, "Toward URLLC: A full duplex relay system with self-interference utilization or cancellation," *IEEE Wireless Commun.*, vol. 28, no. 1, pp. 74–81, Feb. 2021.
[15] P. Aquilina and T. Ratnarajah, "Performance analysis of IA techniques in the MIMO IBC with imperfect CSI," *IEEE Trans. Commun.*, vol. 63, no. 4, pp. 1259–1270, Apr. 2015.
[16] K. Singh, K. Wang, S. Biswas, Z. Ding, F. A. Khan, and T. Ratnarajah, "Resource optimization in full duplex non-orthogonal multiple access systems," *IEEE Trans. Wireless Commun.*, vol. 18, no. 9, pp. 4312–4325, Sep. 2019.
[17] A. C. Cirik, S. Biswas, S. Vuppala, and T. Ratnarajah, "Beamforming design for full-duplex MIMO interference channels–QoS and energy-efficiency considerations," *IEEE Trans. Commun.*, vol. 64, no. 11, pp. 4635–4651, Nov. 2016.
[18] I. P. Roberts and S. Vishwanath, "Beamforming cancellation design for millimeter-wave full-duplex," in *Proc. IEEE Global Commun. Conf. (GLOBECOM)*, Dec. 2019, pp. 1–6.
[19] J. Dai, J. Liu, J. Wang, J. Zhao, C. Cheng, and J.-Y. Wang, "Achievable rates for full-duplex massive MIMO systems with low-resolution ADCs/DACs," *IEEE Access*, vol. 7, pp. 24343–24353, 2019.
[20] S. Wu, C.-X. Wang, E.-H. M. Aggoune, M. M. Alwakeel, and X. You, "A general 3-D non-stationary 5G wireless channel model," *IEEE Trans. Commun.*, vol. 66, no. 7, pp. 3065–3078, Jul. 2018.
[21] I. P. Roberts, H. B. Jain, and S. Vishwanath, "Equipping millimeter-wave full-duplex with analog self-interference cancellation," in *Proc. IEEE Int. Conf. Commun. Workshops (ICC Workshops)*, Jun. 2020, pp. 1–6.
[22] W. Kim and B. Shim, "Ultra-mini slot transmission for 5G+ and 6G URLLC network," in *Proc. IEEE 92nd Veh. Technol. Conf. (VTC-Fall)*, Nov. 2020, pp. 1–5.
[23] Z. Li, M. A. Uusitalo, H. Shariatmadari, and B. Singh, "5G URLLC: Design challenges and system concepts," in *Proc. 15th Int. Symp. Wireless Commun. Syst. (ISWCS)*, Aug. 2018, pp. 1–6.
[24] S. Sadjina, C. Motz, T. Paireder, M. Huemer, and H. Pretl, "A survey of self-interference in LTE-advanced and 5G new radio wireless transceivers," *IEEE Trans. Microw. Theory Techn.*, vol. 68, no. 3, pp. 1118–1131, Mar. 2020.
[25] D. Lee and B.-W. Min, "Demonstration of self-interference antenna suppression and RF cancellation for full duplex MIMO communications," in *Proc. IEEE Wireless Commun. Netw. Conf. Workshops (WCNCW)*, Apr. 2020, pp. 1–4.
[26] A. Balatsoukas-Stimming, A. C. Austin, P. Belanovic, and A. Burg, "Baseband and RF hardware impairments in full-duplex wireless systems: Experimental characterisation and suppression," *EURASIP J. Wireless Commun. Netw.*, vol. 2015, no. 1, pp. 1–11, Dec. 2015.
[27] T. Fukui, K. Komatsu, Y. Miyaji, and H. Uehara, "Analog self-interference cancellation using auxiliary transmitter considering IQ imbalance and amplifier nonlinearity," *IEEE Trans. Wireless Commun.*, vol. 19, no. 11, pp. 7439–7452, Nov. 2020.
[28] S.-A. Ayati, A. Alizadeh, and S. Kiaei, "CMOS full-duplex mixer-first receiver with adaptive self-interference cancellation," *IEEE Trans. Circuits Syst. I, Reg. Papers*, vol. 68, no. 2, pp. 868–878, Feb. 2021.
[29] F. J. Soriano-Irigaray, J. S. Fernandez-Prat, F. J. Lopez-Martinez, E. Martos-Naya, O. Cobos-Morales, and J. T. Entrambasaguas, "Adaptive self-interference cancellation for full duplex radio: Analytical model and experimental validation," *IEEE Access*, vol. 6, pp. 65018–65026, 2018.
[30] X. Lin, A. Grovlen, K. Werner, J. Li, R. Baldemair, J.-F.-T. Cheng, S. Parkvall, D. C. Larsson, H. Koorapaty, M. Frenne, and S. Falahati, "5G new radio: Unveiling the essentials of the next generation wireless access technology," *IEEE Commun. Standards Mag.*, vol. 3, no. 3, pp. 30–37, Sep. 2019.
[31] *5G; Study on Channel Model for Frequencies From 0.5 to 100 GHz (Release 14)*, Standard TR 38.901, 3GPP, 3rd Generation Partnership Project, Sophia Antipolis Cedex, France, 2018.

HAIFENG LUO received the bachelor's degree from the Civil Aviation University of China, in 2018, and the M.S. degree from The University of Edinburgh, Edinburgh, U.K., in 2019, where he is currently pursuing the Ph.D. degree with the Institute for Digital Communications. His research interests include signal processing about 5G and beyond 5G wireless networks, full-duplex radios, and machine-learning-aided communications.

ABHIJEET BISHNU (Member, IEEE) received the B.E. degree in electronics and communication engineering from the Technocrat Institute of Technology, Bhopal, India, in 2010, the M.E. degree in electronics and telecommunication engineering from the Shri Govindram Seksaria Institute of Technology and Science, Indore, India, in 2013, and the Ph.D. degree in electrical engineering from the Indian Institute of Technology Indore, in 2019. He was a Visiting Research Scholar at The University of Edinburgh, U.K., in 2019. He is currently a Postdoctoral Research Associate with The University of Edinburgh. His research interests include channel estimation, cognitive radio, MIMO-OFDM systems, and full-duplex communication. He has served as a reviewer for many IEEE and Springer journals.

THARMALINGAM RATNARAJAH (Senior Member, IEEE) was the Head of the Institute for Digital Communications, from 2016 to 2018. He is currently a Professor of digital communications and signal processing with the Institute for Digital Communications, The University of Edinburgh, Edinburgh, U.K. He has supervised 16 Ph.D. students and 21 postdoctoral research fellows and raised more than 11 million USD of research funding. His research interests include signal processing and information theoretic aspects of 6G wireless networks, full-duplex radio, mmWave communications, random matrices theory, interference alignment, statistical and array signal processing, and quantum information theory. He has published over 400 publications in these areas and holds four U.S. patents. He is a fellow of the Higher Education Academy (FHEA). He was an Associate Editor of IEEE TRANSACTIONS ON SIGNAL PROCESSING, from 2015 to 2017. He was a Technical Co-Chair of the 17th IEEE International workshop on Signal Processing Advances in Wireless Communications, Edinburgh, U.K., July 3–6, 2016.